

**MAGNETIC RECYCLABLE MICROCOMPOSITE SILICA-STEEL  
CORE WITH TiO<sub>2</sub> NANOCOMPOSITE SHELL PHOTOCATALYSTS  
FOR SUSTAINABLE WATER PURIFICATION**

M. Wilson, C. Y. C. Cheng, G. Oswald, R. Srivastava<sup>a</sup>, S. K. Beaumont, and J. P. S.  
Badyal\*

Department of Chemistry  
Science Laboratories  
Durham University  
Durham DH1 3LE  
England, UK

<sup>a</sup> Department of Chemistry, Indian Institute of Technology Ropar, Punjab 140001,  
India

\* Corresponding author email: [j.p.badyal@durham.ac.uk](mailto:j.p.badyal@durham.ac.uk)

## **ABSTRACT**

Micron-sized steel particles encapsulated within a silica host matrix and then coated with a photocatalytic TiO<sub>2</sub> nanocomposite shell have been prepared using sol-gel chemistry and shown to readily degrade waterborne organic pollutants during UV illumination. These silica-steel microcomposite core with TiO<sub>2</sub> nanocomposite shell photocatalysts can be recycled multiple times from solution by magnetic separation.

## **KEYWORDS**

Photocatalysis; nanocomposite; water purification; magnetic recycling; titania.

## 1. INTRODUCTION

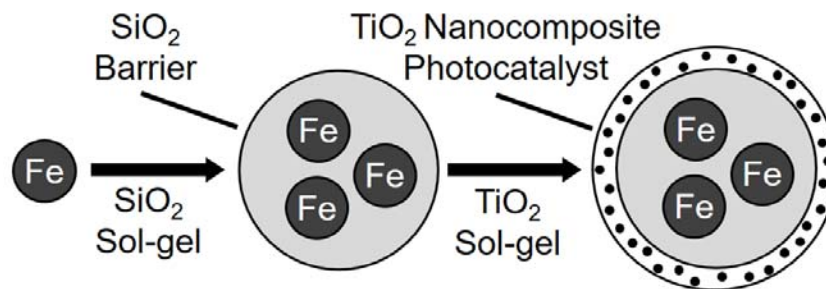
Approximately two billion people worldwide lack access to clean drinking water.<sup>1</sup> In rural regions of developing countries, this is often due to surface or ground water being contaminated with agricultural run-off.<sup>2,3</sup> These pollutants include organic pesticides applied to arable land, travelling from point of application through waterways into river mouths.<sup>4,5,6</sup> Subsequent chronic ingestion can lead to fatal illnesses such as non-Hodgkin's lymphoma and Parkinson's disease.<sup>7,8,9</sup> In particular, children tend to be at high risk due to toxic dosages being as low as 1% advised for adults.<sup>10</sup> Industrialisation is another major source of organic molecule water contamination.<sup>11</sup> Often in developing countries, chloro and aromatic compounds are detected in textile factory effluents.<sup>12,13,14</sup> These environmental pollutants have been linked to mutagenic effects in mammals and aquatic vertebrates.<sup>15,16,17,18</sup>

One potential solution at the local village level (point of use) involves the UV illumination of semiconductor band gap materials (such as  $\text{TiO}_2$ ) for the photocatalytic degradation of organic pesticide and dye pollutants,<sup>19,20,21,22,23</sup> alongside the inherent benefit of high UV bactericidal activity towards *E. coli* and other common waterborne health risks.<sup>24,25,26,27</sup> In particular, the use of  $\text{TiO}_2$  nanoparticles has been widely reported for this purpose, despite such hydrophilic nanoparticles posing a risk to natural ecosystems due to their high levels of aqueous dispersity.<sup>28,29</sup> For instance,  $\text{TiO}_2$  nanoparticles display biological toxicity towards living tissues sensitive to oxidative stress, such as those containing brain microglia and bronchial epithelial cells.<sup>30,31</sup> Furthermore, their small size makes them difficult to remove by physical means (e.g. filtration) because small pore membranes easily become blocked. Therefore, larger size, cheap, and easily separable photocatalytic particles are sought for sustainable water purification applications in developing countries.

$\text{TiO}_2$  coated magnetic core particles are promising candidates for magnetically recoverable photocatalysts. Previous examples for local production include: agglomerated  $\text{TiO}_2$  coated sub-micron size iron oxide particles synthesised from ferric chloride (which is toxic),<sup>32,33</sup> micron-sized magnetic Mn-Zn ferrite photocatalysts prepared from waste materials (which are a cheaper variant, however their synthesis requires an extensive number of wet chemical steps as well as the

handling and disposal of waste sulphuric acid)<sup>34</sup>, the combining TiO<sub>2</sub> particles and a magnetic component within an organic matrix (such as chitosan,<sup>35</sup> poly(methyl methacrylate),<sup>36</sup> or poly(vinyl pyrrolidone))<sup>37</sup> to form micron-sized particles (these suffer from the organic host matrices themselves being vulnerable to photodegradation by the TiO<sub>2</sub> photocatalysts over extended periods of operation)<sup>38,39</sup>, and the utilisation of inorganic matrices, such as reduced graphene oxide,<sup>40</sup> SrFe<sub>12</sub>O<sub>19</sub> nanofibres,<sup>41</sup> or hydrotalcite clays,<sup>42</sup> ( which add significant costs).

A simple, quick, and cheap strategy is described in this article comprising the encapsulation of magnetically separable micron-sized steel filings with a sol-gel TiO<sub>2</sub> nanocomposite photocatalyst shell. Sol-gel chemistry is already widely employed for the large scale manufacture of silica and titania aerogels, nanopowders, and coatings.<sup>43</sup> Typically this involves acid hydrolysis of silica and titania precursors, followed by for example, substrate dipping, and a final thermal curing step.<sup>44,45</sup> This approach offers many advantages, including independent scope for fine tuning particle size,<sup>43</sup> pore size,<sup>46</sup> and film hardness, either by variation of the sol-gel synthesis conditions, or by mixing additional particles (such as photocatalytic P25 TiO<sub>2</sub> nanoparticles).<sup>47</sup> In the present study, micron size magnetic steel particles are first encapsulated within a double sol-gel silica host matrix barrier layer to protect against corrosion, as well as help suppress electron-hole recombination and electron-hole transfer between the TiO<sub>2</sub> outer layer and the underlying steel particles.<sup>48,49</sup> These silica-steel microcomposite particles are then coated with a photocatalytic nanocomposite outer shell comprising photoactive TiO<sub>2</sub> (P25) nanoparticles incorporated within a TiO<sub>2</sub> sol-gel host matrix, Scheme 1. These silica-steel microcomposite core with TiO<sub>2</sub>-P25 nanocomposite shell photocatalysts have been characterised by X-ray photoelectron spectroscopy (XPS), Raman microscopy, X-ray diffraction (XRD), UV-Vis diffuse reflectance spectroscopy, and BET surface area analysis. Photocatalytic degradation rates have been measured using aqueous methylene blue dye solution,<sup>50,51</sup> which is considered to be a good model pollutant for many organic pesticides and dyes which contain aromatic, heteroaromatic, and chloro groups.<sup>6,52,53,54,55</sup>



Scheme 1: Sol-gel preparation of microcomposite silica-steel core with  $\text{TiO}_2$  nanocomposite shell photocatalysts.

## 2. EXPERIMENTAL

### 2.1 Substrate Preparation

Quartz slides (23 mm x 10 mm x 2 mm, cut from a 75 mm diameter quartz window, UQG Ltd.) were cleaned with detergent and then sonicated in propan-2-ol (+99.5 wt%, Fisher Scientific UK Ltd.) for 15 min prior to use as control substrates.

Small pieces of sheet steel (10 mm x 10 mm x 1 mm, ECISS grade S275 (<0.25 wt% C, <1.60 wt% Mn, <0.04 wt% P, <0.05 wt% S, <0.05 wt% Si), SES Multi Metal Stock Ltd.) were used as model flat steel substrates. These were scrubbed with detergent followed by 15 min sonication in propan-2-ol. They were then rinsed with high purity water (BS 3978 Grade 1) and immersed in a 10 wt% solution of sodium hydroxide (99.2 wt%, Fisher Scientific UK Ltd.) in high purity water for 10 min. Next, the steel plates were rinsed in high purity water, and immersed in a solution comprising hydrochloric acid (32 wt% in water, Fisher Scientific UK Ltd.), nitric acid (70 wt% in water, Fisher Scientific UK Ltd.) and high purity water in a volume ratio of 1.0 : 2.0 : 17.0 for 10 min. This was followed by rinsing in high purity water, washing in acetone (+99.8 wt%, Fisher Scientific UK Ltd.), and final removal of surface contaminants by placing in a UV-Ozone cleaner (ProCleaner, BioForce Nanosciences Inc.) for 40 min, ready for coating.

Micron-sized steel particles were ground from a steel rod (ECISS grade S275 (<0.25 wt% C; <1.60 wt% Mn; <0.04 wt% P; <0.05 wt% S; <0.05 wt% Si), SES Multi Metal Stock Ltd.) using a horizontal belt finisher (Bandfacer, RJH Finishing Systems Ltd., running at 0.75 hp) fitted with a sanding belt (180 grit, 100 mm x 915 mm

linishing belt, Deerfos Europe Sp. z.o.o.). The obtained coarse steel particles were magnetically separated from any residual non-magnetic particulates. Next, they were further ground manually under a 2 kg mass (with a cross-sectional area of 65 cm<sup>2</sup>) for 30 min placed between two pieces of dry silicon carbide finishing paper (p400 grit, manufactured by Bibielle S.p.A., supplied by MSC Industrial Supply Co.), followed by grinding down between finer grade dry silicon carbide finishing paper (p1200 grit, Bibielle S.p.A., supplied by MSC Industrial Supply Co.) for 30 min, then magnetically separated and rinsed in acetone to yield a median particle size of 2.9 µm (upper and lower quartiles of 4.2 and 2.2 µm respectively, measured using a light microscope, Model BX40, Olympus Corp.).

A cylindrical glass plasma reactor (5.5 cm diameter, 475 cm<sup>3</sup> volume) housed within a Faraday cage was used for plasma cleaning of the steel particles. This was connected to a 30 L min<sup>-1</sup> rotary pump via a liquid nitrogen cold trap (base pressure less than  $2 \times 10^{-3}$  mbar and air leak rate better than  $6 \times 10^{-9}$  mol s<sup>-1</sup>).<sup>56</sup> A copper coil wound around the glass reactor (4 mm diameter, 11 turns, located 10 cm downstream from the gas inlet) was connected to a 13.56 MHz radio frequency (RF) power supply via an L-C matching network. Prior to loading each batch of steel particles, the whole apparatus was thoroughly scrubbed using detergent and hot water, rinsed with propan-2-ol, oven dried at 150 °C, and further cleaned using a continuous wave 50 W air plasma at 0.2 mbar pressure for 30 min. Next, the steel particles were placed inside the chamber and plasma cleaned using the aforementioned electrical discharge parameters, ready for sol-gel coating application.

## **2.2 Silica Barrier Layer**

A silica barrier layer was applied to the steel particles in order to protect against rusting, as well as suppressing electron-hole recombination, and electron-hole transfer from TiO<sub>2</sub> photocatalyst overlayer to the underlying steel particles.<sup>48,49</sup> A silica sol-gel was prepared by acid catalysed hydrolysis of tetraethyl orthosilicate (TEOS, +98 wt%, Sigma-Aldrich Co. LLC.) through mixing with ethanol (+99.8 wt%, Fisher Scientific UK Ltd.), high purity water, and hydrochloric acid (32 wt% in water, Fisher Scientific UK Ltd.) in a molar ratio of 1.0 : 3.8 : 7.3 :  $5.4 \times 10^{-3}$  respectively

and magnetic stirring at 60 °C for 60 min. The extent of condensation increased with time, where the solution initially consisted of a sol and was followed by the formation of a gel network.<sup>43</sup> In order to produce uniform silica coatings, the sol-gel solutions were used within 48 h of synthesis, whilst the sol-gel remained at its lowest viscosity (typically comprising particles in the nanometre size range).<sup>43</sup>

Coating of steel particles with one layer of silica entailed immersion in the sol-gel followed by vigorous manual agitation every 5 min over a 60 min period in order to ensure uniform particle dispersion throughout the growth phase of the coating. These coated steel particles were then magnetically separated, rinsed with ethanol, dried in air over a hot plate at 80 °C for 15 min, annealed at 150 °C under vacuum (<60 mbar) for 1 h, and finally any large agglomerates were mechanically separated using a ceramic pestle and mortar. Quartz slides and steel plates were also coated using this method (however vigorous agitation and magnetic separation were not necessary). The coated steel plates were analysed by X-ray photoelectron spectroscopy (XPS) in order to check for complete coverage of the steel substrate by the silica layer. Double silica barrier layers were built up by repeating the aforementioned procedure in order to ensure complete coverage of the substrate.

### **2.3 TiO<sub>2</sub> Coating**

A TiO<sub>2</sub> sol-gel was prepared by stirring a solution of the following chemicals for 1 h prior to use: propan-2-ol, glacial acetic acid (+99 wt%, Fisher Scientific UK Ltd.), and titanium isopropoxide (+97 wt%, Sigma-Aldrich Co. LLC.) in a molar ratio of 45.0 : 6.0 : 1.0 respectively. In order to produce uniform coatings of TiO<sub>2</sub>, the sol-gel solutions were used within 48 h of synthesis, whilst the sol-gel remained at its lowest viscosity (typically comprising particles in the nanometre size range).<sup>43</sup>

Quartz slides and steel plates precoated with a double silica barrier layer (to ensure complete coverage of the surface) were dip coated into the TiO<sub>2</sub> sol for 15 s and allowed to dry in air at 20 °C for 30 min. This TiO<sub>2</sub> sol coating cycle was repeated three times for both substrates, in order to build up the layer, followed by air calcination at 500 °C for 30 min using a ramp rate of 5 °C min<sup>-1</sup>.

500–600 mg batches of steel particles precoated with a double silica barrier layer were dip coated by immersion into 2 mL of the TiO<sub>2</sub> sol-gel, manually agitating

for 15 s, followed by magnetic separation whilst decanting the excess solution. These TiO<sub>2</sub> sol-gel coated steel particles were then dried under N<sub>2</sub> (99.998 vol%, BOC Ltd.) flow at 20 °C for 30 min, and any large agglomerates were mechanically separated using a ceramic pestle and mortar. This TiO<sub>2</sub> sol-gel coating cycle was repeated 8 times to build up a sufficiently thick layer, and finally calcined at 500 °C for 30 min using a ramp rate of 5 °C min<sup>-1</sup> under a dry (<60 ppm H<sub>2</sub>O, Series 3 moisture monitor, GE Panametrics Ltd.) gas flow of O<sub>2</sub> (99.5 vol%, BOC Ltd., 20 cm<sup>3</sup> min<sup>-1</sup>) and N<sub>2</sub>. This is designated as one overall TiO<sub>2</sub> coating layer, Table 1. Calcination under gas flow was required due to the higher surface area of steel particle substrates compared to flat steel and quartz substrates. The use of a dry O<sub>2</sub>/N<sub>2</sub> gas mixture was important in order to prevent rusting of the particles.

Table 1: TiO<sub>2</sub> coated substrates (all precoated with a double silica barrier layer).

Sample Code	Substrate	Outer Coating Matrix Material	Number of TiO <sub>2</sub> coating layers
TiO <sub>2</sub> (Q)	Quartz Slide	Sol-Gel TiO <sub>2</sub>	1
TiO <sub>2</sub> (1)	Steel Particles	Sol-Gel TiO <sub>2</sub>	1

#### 2.4 Nanocomposite TiO<sub>2</sub> Photocatalytic Coatings

3.6 wt% Aeroxide® P25 TiO<sub>2</sub> nanoparticles (anatase : rutile ratio 80 : 20 wt%, BET surface area 50 m<sup>2</sup> g<sup>-1</sup>, Acros Organics)<sup>57</sup> were added to a freshly prepared TiO<sub>2</sub> sol-gel comprising a solution of propan-2-ol, glacial acetic acid and titanium isopropoxide in molar ratios of 45.0 : 6.0 : 1.0 respectively, which had been stirred for 1 h prior to use.

Quartz slides coated with a double silica barrier layer were dip coated into the TiO<sub>2</sub>-P25 nanocomposite sol-gel for 15 s followed by drying in air at 20 °C. This cycle was repeated three times followed by air calcination at 500 °C for 30 min, using a ramp rate of 5 °C min<sup>-1</sup>.

500–600 mg batches of steel particles coated with a double silica barrier layer were dip coated by immersion into 2 mL of the TiO<sub>2</sub>-P25 nanocomposite sol-gel and manually agitated for 15 s, followed by magnetic separation whilst decanting the excess solution. These TiO<sub>2</sub>-P25 nanocomposite sol-gel coated steel particles were

then dried under N<sub>2</sub> flow at 20 °C for 30 min, and any large agglomerates were mechanically separated using a ceramic pestle and mortar. This TiO<sub>2</sub>-P25 nanocomposite sol-gel coating cycle was repeated 8 times to build up a sufficiently thick layer, and finally calcined at 500 °C for 30 min using a ramp rate of 5 °C min<sup>-1</sup> under a dry (<30 ppm H<sub>2</sub>O) gas flow of O<sub>2</sub> (20 cm<sup>3</sup> min<sup>-1</sup>) and N<sub>2</sub> (80 cm<sup>3</sup> min<sup>-1</sup>). This is designated as one overall TiO<sub>2</sub>-P25 nanocomposite coating layer, Table 2.

Table 2: TiO<sub>2</sub>-P25 nanocomposite coated substrates (all precoated with a double silica barrier layer). Total coating thicknesses measured by: (†) optical microscopy; and (‡) Raman microscopy.

Sample Code	Substrate	Matrix Material	Filler Nanoparticles	Number of TiO <sub>2</sub> -P25 Nanocomposite Coating Layers	Total Coating Thickness / μm
P25(Q)	Quartz Slide	Sol-Gel TiO <sub>2</sub>	P25 TiO <sub>2</sub>	1	2.75 ± 0.25 <sup>†</sup>
P25(1)	Steel Particles	Sol-Gel TiO <sub>2</sub>	P25 TiO <sub>2</sub>	1	6 ± 2 <sup>‡</sup>
P25(3)	Steel Particles	Sol-Gel TiO <sub>2</sub>	P25 TiO <sub>2</sub>	3	10 ± 4 <sup>‡</sup>
P25(5)	Steel Particles	Sol-Gel TiO <sub>2</sub>	P25 TiO <sub>2</sub>	5	27 ± 8 <sup>‡</sup>

## 2.5 Characterization

Silica adhesion layer thicknesses on quartz slides were determined by cryo-fracturing coated slides using liquid nitrogen, and subsequent analysed by scanning electron microscopy (SEM, VEGA3 LMU, Tescan Orsay Holding, a.s.) at 25 kV, with sample cross sections orientated 10° from parallel to the beam path.

TiO<sub>2</sub> coating thickness on quartz slides was measured by confocal laser scanning microscopy (LSM 880 with Airyscan, Carl Zeiss AG) by analysing 22 μm x 22 μm areas of coating. Reflectance of the TiO<sub>2</sub> sol-gel and TiO<sub>2</sub>-P25 nanocomposite sol-gel coatings under laser light (wavelength of 405 nm, transmitted by the quartz substrate and silica barrier layer) was captured in cross-sections parallel to the coating's surface. Image stack acquisition was started from above the surface of the coating and then moving in 0.29 μm steps along the direction perpendicular to the coating, using a 0.60 μm thickness optical section. Image stacks were rotated to yield the coating cross-section, and the average thickness of the film

was then calculated by measuring the cross sectional area (ImageJ) and dividing it by the section length.

Surface elemental compositions were measured by X-ray photoelectron spectroscopy (XPS) using a VG ESCALAB II electron spectrometer equipped with a non-monochromated Mg  $K\alpha_{1,2}$  X-ray source (1253.6 eV) and a concentric hemispherical analyser. Photoemitted electrons were collected at a take-off angle of  $20^\circ$  from the substrate normal, with electron detection in the constant analyser energy mode (CAE, pass energies of 20 and 50 eV for high resolution and survey spectra respectively). Experimentally determined instrument sensitivity factors were taken as C(1s) : O(1s) : Si(2p) : Fe(3d) equals 1.00 : 0.35 : 0.97 : 0.09 respectively.

Raman spectra were acquired on a confocal microscope laser Raman system (model Labram 1B, Instruments S. A. (UK) Ltd.) equipped with a 15 mW He-Ne laser (6328 Å) excitation source and an air cooled CCD detector (model SpectrumOne CCD 2000). For Raman spectroscopy, coated steel and reference particle samples were compressed and levelled into a glass sample cell (10 mm diameter and 2 mm depth). Spectral background subtraction utilised a 6<sup>th</sup> degree polynomial. For Raman microscopy analysis, samples were set into epoxy resin (5 : 2 mixture of Epoxy resin L : Hardener S, R&G Faserverbundwerkstoffe GmbH Composite Technology) at 1 wt%, cured for 24 h at room temperature ( $20^\circ\text{C}$ ), then cross sectioned using sequential polishing with dry silicon carbide finishing paper (p400 and p1200 grit, manufactured by Bibielle S.p.A., supplied by MSC Industrial Supply Co.) and alumina metal polish (Solvol®, Autosol LLC.). Raman microscopy spectra were taken at 1  $\mu\text{m}$  intervals along a linear trace through the centre of each analysed particle using a 1800 g/mm grating; subsequently, Raman microscopy profiles were generated from the area of the anatase Eg  $\text{TiO}_2$  ( $594\text{--}691\text{ cm}^{-1}$ ) and haematite  $\text{Fe}_2\text{O}_3$  ( $262\text{--}310\text{ cm}^{-1}$ ) signals. A  $\text{TiO}_2$  coating thickness for each analysed particle was calculated by averaging the distance measured between the outer and inner boundaries of the anatase Eg signal on each edge of the cross-sectioned particle.

X-ray diffractograms were obtained across  $5^\circ\text{--}80^\circ$   $2\theta$  range with  $0.02^\circ$  step size using a powder diffractometer (model d8, Bruker Corp.). The copper anode X-ray source was operated at 40 kV and 40 mA emitting Cu  $K\alpha$  1.5418 Å wavelength radiation.

UV-Vis absorbance spectra of coated quartz slides were acquired using a custom built centre-mount low density PTFE integrating sphere with an internal

diameter of 100 mm. Illumination was provided from a deuterium tungsten-halogen fibre optic source (model DH-2000-S, Ocean Optics Inc., 215–2500 nm range), and the reflected light was analysed by a fibre coupled CCD spectrophotometer (200–850 nm range, model USB-2000+, Ocean Optics Inc.).

Particle sizes were measured using a light microscope (Model BX40, Olympus Corp.). Particle surface area was determined using the BET method<sup>58</sup> (model BET-201 sorptometer, PMI Inc.). Prior to recording nitrogen adsorption isotherms, the samples (100–200 mg) were degassed under vacuum (<0.05 mbar) at 200 °C for 3 h.

## **2.6 Photocatalytic Testing of Coated Steel Particles**

TiO<sub>2</sub> photocatalyst coated silica-steel microcomposite core particles (solution concentration of  $2.0 \pm 0.3 \text{ mg mL}^{-1}$ ) were tested in a 100 mL volume cylindrical borosilicate glass reaction vessel (fitted with a quartz window for UV irradiation) filled with 90 mL of a 4.0  $\mu\text{M}$  aqueous solution of methylene blue dye (+70 wt%, TCL UK Ltd.), Figure 1. Particles were agitated using a vertically mounted magnetic stirrer hot plate (IKAMAG RCT, IKA<sup>®</sup>-Werke GmbH & Co. KG) in contact with the back face of the reactor, and oxygen dissolution was maintained via a glass diffuser bubbling oxygen at a flow rate of  $5 \text{ cm}^3 \text{ min}^{-1}$  at 1.5 Bar pressure. A Hg-Xe short arc lamp (model 6136, 200 W rated, operating at 26 V and 7 A, Oriel Newport Corp.) positioned 15 cm away from the reactor quartz window provided an incident UV flux of  $7.4 \pm 1.4 \text{ mW cm}^{-2}$  onto the solution (measured with a thermopile and digital voltmeter, model 5300, Applied Photophysics Ltd.). A contact thermometer was used as part of a feedback loop to the stirrer hot plate in order to maintain the reaction vessel temperature at  $28 \pm 2 \text{ }^\circ\text{C}$ . Prior to UV irradiation, the photocatalyst coated steel particles were allowed to equilibrate in the methylene blue dye solution for 1 h in order to determine the extent of methylene blue dye adsorption onto the coated steel particles. 1 mL aliquots, filtered through a 0.22  $\mu\text{m}$  polyethersulfone syringe filter (Gilson Scientific Ltd.), were taken prior to the addition of photocatalyst, and at 10 min intervals during UV illumination for UV-Vis absorption spectroscopy analysis of methylene blue dye concentrations at  $\lambda_{\text{max}} = 660 \text{ nm}$  (model UV4, Unicam Lda.).<sup>59</sup> Dye photodegradation rate constants were calculated from absorbance readings

taken over 1 h of UV exposure assuming first order kinetics (over this period dye degradation did not reach a point where mass transfer and other effects caused a deviation from linearity of the plots).<sup>50,51</sup> UV degradation of methylene blue dye in the absence of coated steel particles served as a control (the measured rate constant of  $5.9 \pm 1.5 \times 10^{-3} \text{ min}^{-1}$  was subtracted for each set of photocatalysis experiments). The calculated rate was then normalised to the surface area of the photocatalyst coated steel particles. Finally, the ease of recycling was demonstrated by using a hand magnet to separate coated steel particles aqueous solution between consecutive photocatalytic cycles.

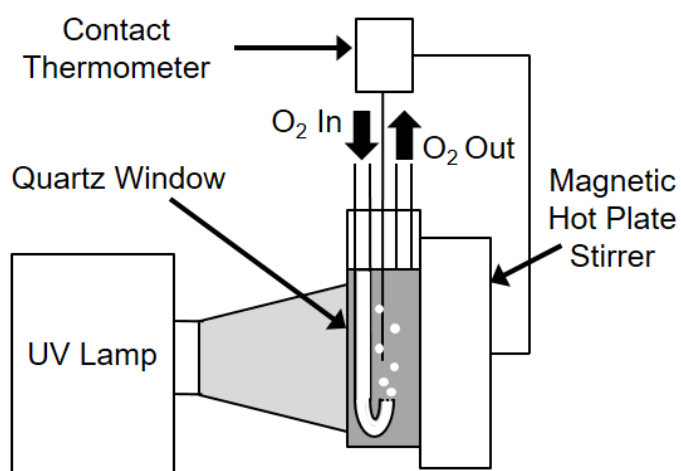


Figure 1: Schematic of borosilicate glass photoreactor fitted with a quartz front window and magnetic hot plate stirrer.

### 3. RESULTS

#### 3.1 Silica Barrier Layer

Wide scan XPS survey spectra of uncoated steel plates indicated the presence of only iron, oxygen, and carbon species at the surface (1–2 nm sampling depth),<sup>60,61</sup> Figure 2. The O(1s) envelope could be fitted to two different oxygen atom environments corresponding to bulk lattice  $\text{Fe}_2\text{O}_3$  ( $530.7 \pm 0.1 \text{ eV}$ ),<sup>62,63</sup> and surface hydroxyl groups ( $532.3 \pm 0.1 \text{ eV}$ ).<sup>62,64</sup> Deposition of a double silica barrier layer was found to be necessary to achieve complete coverage of the steel substrate, as

confirmed by the disappearance of the iron XPS features in conjunction with the emergence of signals from silicon containing species. This included the appearance of a higher binding energy O(1s) component ( $533.1 \pm 0.1$  eV) characteristic of silica lattice and silanol groups.<sup>65,66</sup>

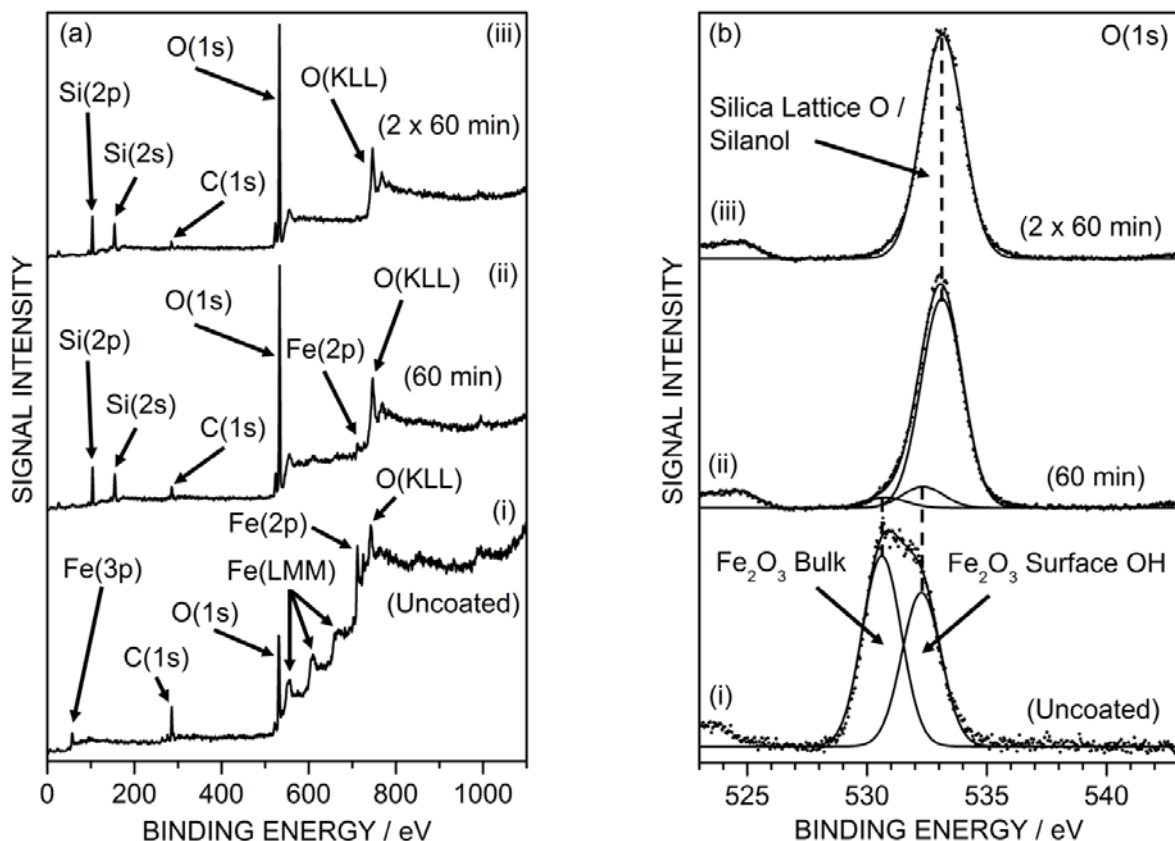


Figure 2: XPS spectra: (a) wide scan survey spectra of: (i) clean uncoated steel plate; (ii) single silica barrier layer (60 min deposition) coated steel plate; and (iii) double silica barrier layer (2 x 60 min deposition) coated steel plate; and (b) O(1s) spectra of steel plates: (i) clean uncoated; (ii) single silica barrier layer (60 min deposition); and (iii) double silica barrier layer (2 x 60 min deposition).

Cross-section SEM analysis of the double silica barrier layer deposited onto quartz slides indicated a coating thickness of  $92 \pm 8$  nm, Figure S1, whilst the particle size measured using an optical microscope after double silica barrier layer coating of steel particles (median  $17.7 \mu\text{m}$ ) was an order of magnitude larger compared to uncoated steel particles (median  $2.9 \mu\text{m}$ ). This is consistent with individual double silica barrier layer coated steel particles agglomerating to form larger (more easily handleable) composite particles, Scheme 1.

The Raman spectrum of clean steel particles displayed signals characteristic of haematite ( $\text{Fe}_2\text{O}_3$ ) and magnetite ( $\text{Fe}_3\text{O}_4$ ),<sup>67</sup> Figure 3 and Table S1. An attenuation of these features was observed following application of the double silica barrier layer, accompanied by the emergence of silica peaks ( $993\text{ cm}^{-1}$ ,  $1353\text{ cm}^{-1}$ , and a broad band at around  $3000\text{ cm}^{-1}$ ).<sup>68,69,70</sup> The sampling depth of visible light Raman spectroscopy (which ranges from  $3\text{ }\mu\text{m}$  for pure silicon to over  $20\text{ }\mu\text{m}$  for some metal oxides)<sup>71,72</sup> is of the same magnitude as the double silica barrier layer-steel composite particle sizes (median  $17.7\text{ }\mu\text{m}$ ), resulting in both the silica coating and underlying steel particles being detected.

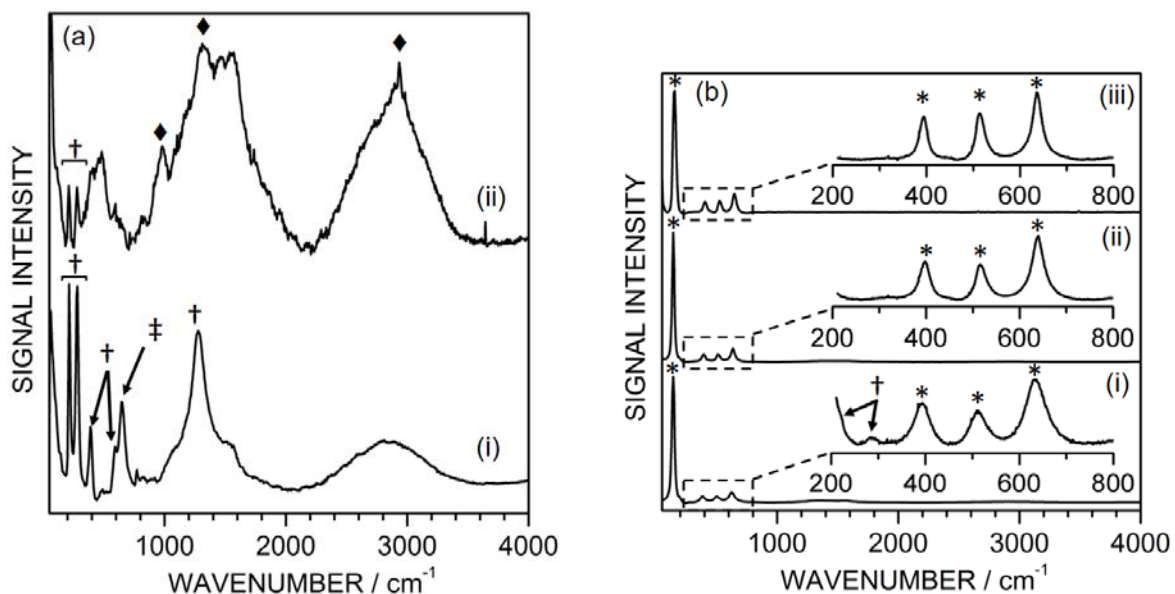


Figure 3: Raman spectra of: (a) steel particles: (i) uncoated; and (ii) double silica barrier layer coated; and (b): (i)  $\text{TiO}_2(1)$  coated silica-steel microcomposite core particles; (ii) P25(5) coated silica-steel microcomposite core particles; and (iii) P25  $\text{TiO}_2$  nanoparticles. Significant peaks labelled: haematite  $\text{Fe}_2\text{O}_3$  ( $\dagger$ ), magnetite  $\text{Fe}_3\text{O}_4$  ( $\ddagger$ ), silica ( $\blacklozenge$ ), and anatase  $\text{TiO}_2$  (\*). Insets in (b) correspond to magnification of the  $200\text{--}800\text{ cm}^{-1}$  region. For coating nomenclature see Table 1 and Table 2.

### 3.2 $\text{TiO}_2$ Coating

Prior to calcination of sol-gel coated  $\text{TiO}_2(1)$  silica-steel microcomposite core particles, Raman spectroscopy indicated that the coating was non-crystalline, with an absence of anatase or rutile Raman signals,<sup>73,74,75,76</sup> Figure S2. Following

calcination of TiO<sub>2</sub>(1) coated steel particles, Raman spectroscopy and powder XRD displayed strong anatase TiO<sub>2</sub> features,<sup>73,74</sup> Figure 3 and Figure 4. Rutile TiO<sub>2</sub> phase was not detected by XRD, which is consistent with the lack of asymmetry in the Raman B<sub>1g</sub> at 386 cm<sup>-1</sup> and E<sub>g</sub> at 621 cm<sup>-1</sup> anatase signals.<sup>73,75,76</sup> Optical particle size analysis showed that the TiO<sub>2</sub> coating steps did not lead to agglomeration.

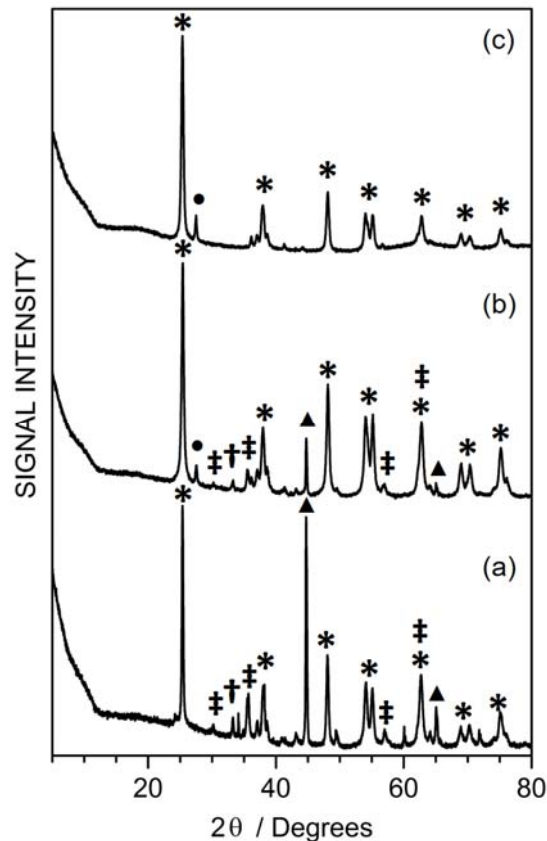


Figure 4: Powder XRD of: (a) TiO<sub>2</sub>(1) coated silica-steel microcomposite core particles; (b) P25(5) coated silica-steel microcomposite core particles; and (c) P25 TiO<sub>2</sub> nanoparticles. Significant diffraction peaks labelled:  $\alpha$ -Fe ( $\blacktriangle$ ); haematite Fe<sub>2</sub>O<sub>3</sub> ( $\dagger$ ); magnetite Fe<sub>3</sub>O<sub>4</sub> ( $\ddagger$ ); anatase TiO<sub>2</sub> (\*); and rutile TiO<sub>2</sub> ( $\bullet$ ).

### 3.3 Nanocomposite TiO<sub>2</sub> Coatings

Powder XRD analysis of P25 TiO<sub>2</sub> nanoparticles showed anatase and rutile polymorph peaks at 2 $\theta$  values of 25.3° (101) and 27.5° (110) respectively, Figure 4.<sup>77,78</sup> The  $[I_{Rutile}] / [I_{Anatase}]$  peak height intensity ratio of 0.10 (corrected for linear background subtraction) was used to calculate an anatase weight fraction ( $W_{Anatase}$ ) of 0.86 using Eq. (1),<sup>79</sup> which is comparable with the previously reported value of  $W_{Anatase} = 0.8$  for P25 TiO<sub>2</sub> material.<sup>57</sup> Additional lower intensity anatase peaks

include  $2\theta$  values of:  $37.8^\circ$ ,  $48.0^\circ$ ,  $53.9^\circ$ ,  $62.7^\circ$ ,  $68.7^\circ$ , and  $74.9^\circ$ .<sup>77,78</sup> Powder XRD analysis of P25(5) coated silica-steel microcomposite core particles detected strong anatase  $\text{TiO}_2$  peaks as well as weak signals from  $\alpha\text{-Fe}$ , haematite ( $\text{Fe}_2\text{O}_3$ ), magnetite ( $\text{Fe}_3\text{O}_4$ ), and rutile  $\text{TiO}_2$ .<sup>77,78,80,81</sup> This is consistent with there being P25  $\text{TiO}_2$  nanoparticles embedded within the  $\text{TiO}_2(1)$  shell coating, Figure 4. For the P25(5) coated silica-steel microcomposite core particles, the sol-gel  $\text{TiO}_2$  : P25  $\text{TiO}_2$  nanoparticle ratio is estimated to be 1.0 : 2.5, by calculating the remaining sol-gel  $\text{TiO}_2$  contribution to  $[I_{\text{Anatase}}]$  after subtracting the P25  $\text{TiO}_2$  nanoparticle contribution (calculated by using the  $[I_{\text{Rutile}}]$  intensity which is taken to be solely due to P25  $\text{TiO}_2$ , in combination with the previously calculated anatase weight fraction ( $W_{\text{Anatase}} = 0.86$ ) for P25  $\text{TiO}_2$  nanoparticles).

$$W_{\text{Anatase}} = 1 / [1 + (1.26[I_{\text{Rutile}}] / [I_{\text{Anatase}}])] \quad \text{Equation (1)}$$

Raman spectroscopy of P25  $\text{TiO}_2$  nanoparticles displayed strong bands associated with anatase  $\text{TiO}_2$  at  $148\text{ cm}^{-1}$ ,  $394\text{ cm}^{-1}$ ,  $513\text{ cm}^{-1}$ , and  $636\text{ cm}^{-1}$ ,<sup>73,74</sup> Figure 3 and Table S1. The lack of any  $\text{TiO}_2$  rutile signal is consistent with previous Raman studies.<sup>82,83</sup> This is most likely due to the inherently low proportion of rutile (around 10 wt%, as shown by XRD) and the overlap of the Raman rutile  $E_g$  and  $A_{1g}$  peaks with the anatase  $B_{1g}$  and  $E_g$  peaks.<sup>73,74,75,76</sup> In the case of P25(5) nanocomposite coated silica-steel microcomposite particles, characteristic anatase  $\text{TiO}_2$  Raman signals were observed, whilst the lack of any significant haematite  $\text{Fe}_2\text{O}_3$  peaks,<sup>67</sup> corroborated a thicker coating compared to  $\text{TiO}_2(1)$ , Figure 3 and Table S1. The absence of any  $\text{TiO}_2$  rutile Raman signal for P25(5), is consistent with the aforementioned reference spectrum of P25  $\text{TiO}_2$  nanoparticles. However, powder XRD enabled a clear distinction to be made between the rutile and anatase phases for P25(5) nanocomposite coated silica-steel microcomposite core particles through the easily resolvable rutile diffraction peak at a  $2\theta$  value of  $27.5^\circ$ , Figure 4. Raman microscopy of cross-sectioned silica-steel microcomposite core with  $\text{TiO}_2$ -P25 nanocomposite shell coating particles was able to identify the different material phases, and confirmed the presence of multiple (agglomerated) steel particles within the core silica host matrix, Figure 5. In contrast, to the earlier double silica barrier layer coating step of the steel particles (median  $17.7\text{ }\mu\text{m}$ ) which resulted in

agglomeration, the sol-gel TiO<sub>2</sub> nanocomposite coating step did not cause agglomeration of the silica-steel microcomposite core particles, Figure 5.

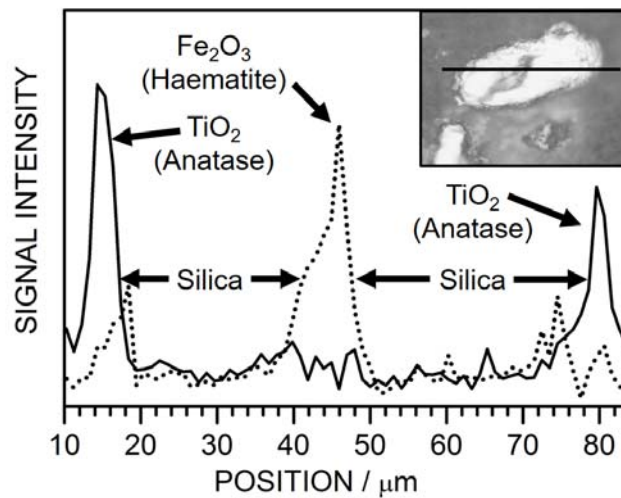


Figure 5: Raman microscopy signal across a cross-sectioned P25(1) coated silica-steel microcomposite core particle: anatase TiO<sub>2</sub> Eg signal (594–691 cm<sup>-1</sup>, solid line); and haematite Fe<sub>2</sub>O<sub>3</sub> signal (262–310 cm<sup>-1</sup>, dotted line). Note haematite signal shows the incorporation of more than one steel particle within the silica-steel microcomposite core. Inset shows the optical micrograph of the particle analysed.

UV-Vis absorption spectra of TiO<sub>2</sub>(Q) and P25(Q) coated quartz slides display distinct band gaps with negligible absorbance at wavelengths exceeding 400 nm into the visible region, Figure 6. The measured band gap of 3.15 eV (393 nm) for TiO<sub>2</sub>(Q) coating is consistent with anatase TiO<sub>2</sub> phase (literature band gap of 3.15–3.20 eV).<sup>77,84</sup> In the case of P25(Q) coating, the lower band gap of 3.08 eV (402 nm) is in good agreement with previous reported values for P25 TiO<sub>2</sub> nanoparticles (3.1 eV),<sup>77,85</sup> which correlates to the larger rutile content measured by powder XRD analysis for P25(5) compared to TiO<sub>2</sub>(1), Figure 4. Furthermore, this incorporation of P25 TiO<sub>2</sub> nanoparticles into TiO<sub>2</sub> sol-gel coatings (P25(Q)), enhances absorbance at shorter wavelengths (energies greater than the band gap), and slightly attenuates absorbance at longer wavelengths (energies below the band gap) compared to TiO<sub>2</sub>(Q), Figure 6. The former can be attributed to a greater amount of absorbing species from a thicker TiO<sub>2</sub> layer (2.75 ± 0.25 μm for P25(Q) compared to 0.79 ± 0.08 μm for TiO<sub>2</sub>(Q) measured by optical microscopy).<sup>86</sup> The latter may stem from differences in band tailing defect states.<sup>87</sup>

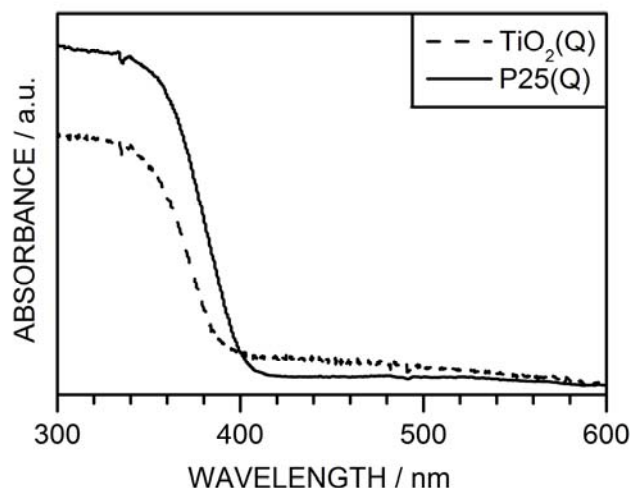


Figure 6: UV-Vis absorbance spectra of coated quartz slides: sol-gel  $\text{TiO}_2$  coating ( $\text{TiO}_2(\text{Q})$ , dashed line); and sol-gel  $\text{TiO}_2$  containing P25 nanoparticles ( $\text{P25}(\text{Q})$ , solid line).

The low surface area of  $0.13 \pm 0.02 \text{ m}^2 \text{ g}^{-1}$  measured for uncoated steel particles is in good agreement with the estimated theoretical surface area of  $0.27 \text{ m}^2 \text{ g}^{-1}$  calculated from the optical particle size distribution (assuming spherical particles and an experimentally determined mild steel density of  $7.53 \pm 0.25 \text{ g m}^{-3}$ ), Table 3.  $\text{TiO}_2$  sol-gel coating of the silica-steel microcomposite particles ( $\text{TiO}_2(1)$ ) increased the overall surface area, whilst corresponding  $\text{TiO}_2$ -P25 nanocomposite shell coated steel-silica microcomposite particles yielded the highest values, with an enhancement factor of over 100 compared to uncoated steel particles being achieved for P25(3) and P25(5) variants, Table 3. This shows that the  $\text{TiO}_2$  layer is porous.

Table 3: Coated steel particle  $\text{TiO}_2$  shell thickness values measured by cross-section Raman microscopy and BET isotherm surface areas.

Steel Particle Coating	$\text{TiO}_2$ Coating Thickness / $\mu\text{m}$	Surface Area / $\text{m}^2 \text{ g}^{-1}$
Uncoated	-	$0.13 \pm 0.02$
$\text{TiO}_2(1)$	$5 \pm 6$	$4.39 \pm 1.32$
P25(1)	$6 \pm 2$	$10.3 \pm 1.9$
P25(3)	$10 \pm 4$	$14.7 \pm 1.5$
P25(5)	$27 \pm 8$	$16.3 \pm 1.7$

### 3.4 Magnetic Recycling Photocatalysis

Following immersion of TiO<sub>2</sub> coated silica-steel microcomposite particles into solution, a preliminary drop in detected methylene blue dye concentration was observed in darkness, Figure 7. This can be attributed to surface adsorption of dye reaching a plateau over a period of about 1 h. Subsequent UV illumination led to photocatalytic dye degradation. For recycling studies, the TiO<sub>2</sub>-silica-steel multicomposite particles were magnetically removed from the solution between each UV exposure cycle. For instance, the first order rate constant for UV photodegradation of the dye was measured to be  $2.31 \pm 0.14 \times 10^{-2} \text{ min}^{-1}$  for the P25(3) photocatalyst during its fifth UV exposure recycle run; this value dropped to  $0.73 \pm 0.23 \times 10^{-2} \text{ min}^{-1}$  following magnetic removal of the photocatalyst particles (which is the same within error as measured in the control experiment using no TiO<sub>2</sub>-silica-steel multicomposite particles ( $0.59 \pm 0.15 \times 10^{-2} \text{ min}^{-1}$ ), thereby ruling out photocatalyst leaching into solution). No visible change or rust was seen on these samples (with the silica double barrier layer) after 5 cycles. Control experiments showed that uncoated steel particles display a photocatalytic dye degradation rate constant of  $0.43 \pm 0.15 \times 10^{-2} \text{ min}^{-1}$ , which lies within the error range of background UV photodegradation (rate constant of  $0.59 \pm 0.15 \times 10^{-2} \text{ min}^{-1}$  in the absence of any particles). Furthermore, TiO<sub>2</sub> or TiO<sub>2</sub>-P25 nanocomposite shell coated silica-steel microcomposite photocatalysts prepared without the interfacial silica double barrier layer led to rapid delamination of the photocatalyst coating upon immersion into methylene blue dye solution, culminating in the formation of rust visible to the naked eye.

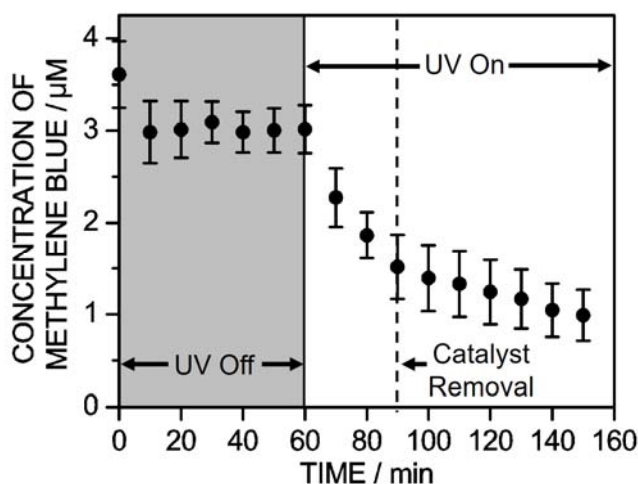


Figure 7: UV photocatalytic degradation profile of methylene blue dye solution ( $4 \mu\text{M}$ ) using P25(3) coated silica-steel microcomposite particles ( $2.0 \pm 0.3 \text{ mg mL}^{-1}$  loading) during the fifth recycle run. Photocatalyst was magnetically removed after 30 min UV exposure, and the resulting methylene blue dye solution was exposed to UV for a further 60 min in the absence of photocatalyst.

First order rate constants (normalised to surface area) for the photodegradation of methylene blue dye solution during 1 h UV illumination were compared across the range of  $\text{TiO}_2$  coated silica-steel microcomposite particle photocatalysts, Figure 8.  $\text{TiO}_2(1)$  shell coating displayed a lower rate constant compared to the  $\text{TiO}_2$ -P25 nanocomposite shell photocatalysts, with the highest rate constant being observed for triple coated sample (P25(3),  $1.55 \pm 0.25 \times 10^{-2} \text{ min}^{-1} \text{ m}^{-2}$  leading to  $92 \pm 5\%$  dye degradation after 1 h UV irradiation ( $82 \pm 4\%$  after 30 min)). Additional  $\text{TiO}_2$ -P25 nanocomposite coating layers led to no further gain in photocatalytic activities. This can be explained in terms of the limited penetration depth of UV photons into  $\text{TiO}_2$  (140 nm),<sup>88</sup> which is significantly less than the coating thicknesses measured for all of the  $\text{TiO}_2$ -P25 nanocomposite shell photocatalysts, Table 3. The surface area normalised rate constants indicate that there is a definite enhancement in the photocatalytic activity through the incorporation of P(25)  $\text{TiO}_2$  nanoparticles into the sol-gel  $\text{TiO}_2$  shell coatings, whilst the total surface area appears to be the main factor contributing to dye photodegradation rates (within error) between the P25(1), P25(3), and P25(5)  $\text{TiO}_2$  nanocomposite coatings, Table 3 and Figure 8.

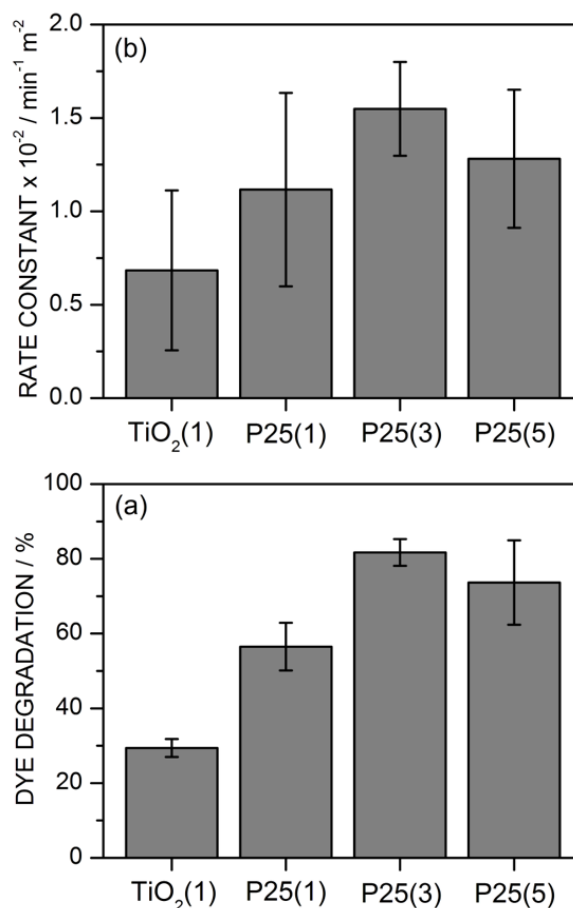
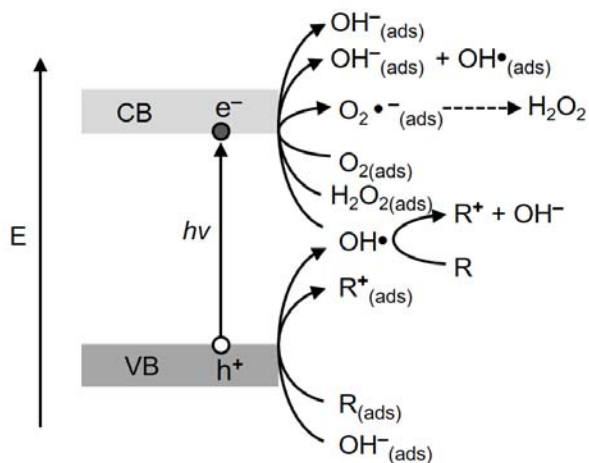


Figure 8: UV degradation of methylene blue dye solution (4  $\mu\text{M}$ ) using TiO<sub>2</sub> photocatalyst coated silica-steel microcomposite core particles (loadings of  $2.0 \pm 0.3 \text{ mg mL}^{-1}$ ): (a) percentage of dye degraded after 30 min continuous UV irradiation; and (b) dye degradation rate normalised to surface area (the large error values are due to propagation of error from surface area measurements). All photodegradation rates of the methylene blue dye solution by the photocatalyst particles were measured following an initial equilibration period in the dark for 1 h (see Figure 7). The background UV degradation rate ( $0.59 \pm 0.15 \times 10^{-2} \text{ min}^{-1}$ ) of methylene blue dye measured in the absence of any photocatalyst particles has been subtracted prior to surface area normalisation in all cases. For reference, dispersed P25 TiO<sub>2</sub> nanoparticles gave a surface area normalised dye photodegradation rate of  $18.7 \pm 2.0 \times 10^{-2} \text{ min}^{-1} \text{ m}^{-2}$  (however, the use of P25 TiO<sub>2</sub> nanoparticles alone for water purification suffers from problems of environmental leaching and difficulty for reuse).

Magnetic separation recycling experiments were conducted on the most promising TiO<sub>2</sub> nanocomposite coated silica-steel microcomposite core particles (P25(3) and P25(5)). These did not display any change in photocatalytic activity (surface area corrected rate constant) over four recycle iterations, Figure S3. Percentage degradation of the methylene blue dye after 30 min of UV exposure for each photocatalyst during recycling displayed a similar trend. Thereby demonstrating the viability of these TiO<sub>2</sub>-P25 nanocomposite coated silica-steel microcomposite core particles as magnetically recyclable photocatalysts.

#### 4. DISCUSSION

TiO<sub>2</sub> photocatalytic degradation of organic pollutants is widely understood to proceed via two predominant reaction pathways: firstly, by highly reactive hydroxyl radicals (originating from photoinduced lattice holes) reacting with pollutant molecules, and secondly by direct electron transfer between pollutant molecules and holes, Scheme 2. In competition with these photodegradative chemical processes, concurrent charge recombination and hydroxyl radical quenching to hydroxide anions takes place (e.g. by photogenerated electrons).<sup>89,90</sup> Adsorbed molecular oxygen also contributes to the overall photodegradation quantum yields.<sup>91</sup> This encompasses electron-hole pairs generated following the onset of UV illumination either undergoing recombination within the bulk, or electrons being trapped by defects and adsorbed surface species (such as molecular oxygen).<sup>92,93,94</sup> The hindering of surface charge recombination through electron trapping by adsorbed molecular oxygen increases hole formation, which in turn enhances reactive hydroxyl radical production.<sup>89,95</sup>



Scheme 2: Important reaction pathways during TiO<sub>2</sub> photocatalyst degradation of organic molecules (R).<sup>96,97,98,99</sup>

In the case of the present organic dye degradation study using silica-steel microcomposite core with TiO<sub>2</sub> shell photocatalyst, any direct interaction between steel particle surface iron oxides and the TiO<sub>2</sub> shell could potentially diminish photocatalytic activity in at least two ways. Firstly, by electron-hole recombination processes through transfer of photogenerated electrons and holes from the TiO<sub>2</sub>

coating to the respective conduction and valence bands of the interfacial iron oxide (the smaller band gap of iron oxides compared to  $\text{TiO}_2$  accelerates the recombination rate, and thus attenuates photocatalytic activity<sup>49</sup>).<sup>100</sup> Secondly, photogenerated electrons in the  $\text{TiO}_2$  layer can migrate towards the underlying interface and reduce lattice  $\text{Fe}^{3+}$  ions to form the more soluble  $\text{Fe}^{2+}$  ions, thereby triggering photodissolution of  $\text{TiO}_2$  coatings.<sup>49</sup> Such dissolved  $\text{Fe}^{2+}$  species are then able to react with hydroxyl radicals leading to a quenching of photocatalytic activity.<sup>101</sup> These unfavourable interactions between the steel particle iron oxide surface layer and the  $\text{TiO}_2$  shell coating can be blocked by utilising a silica interfacial barrier layer.<sup>48,49</sup> A double silica barrier layer was found to be sufficient to block photocatalyst dissolution, as evidenced by the photocatalyst stability over extended magnetic recycling studies, Figure S3.

Despite rutile being the thermodynamically more stable bulk phase, sol-gel processing tends to favour the anatase phase.<sup>102</sup> This can be attributed to the lower surface energy of anatase driving its preferential formation due to the large surface area to bulk volume ratio of the small particles typically formed during sol-gel processing.<sup>103,104,105,106</sup> Additional factors, such as the precursors employed and reaction conditions can also influence  $\text{TiO}_2$  crystal growth.<sup>107,108</sup> The predominance of anatase  $\text{TiO}_2$  in the sol-gel coatings employed in the present study (only a small amount of rutile polymorph found in P25(5)) is consistent with previous sol-gel  $\text{TiO}_2$  calcination studies carried out at below  $700\text{ }^\circ\text{C}$ ,<sup>45</sup> and  $\text{TiO}_2$ -P25 nanocomposite coatings deposited onto glass and flat steel substrates.<sup>47,109</sup>

The high photocatalytic activity reported for P25  $\text{TiO}_2$  nanoparticles is understood to be due to a combination of a large anatase (more photocatalytically active) to rutile ratio plus an inherent grain boundary structure.<sup>110,111</sup> In the present study the incorporation of P25  $\text{TiO}_2$  nanoparticles into the host  $\text{TiO}_2$  sol-gel coating to form  $\text{TiO}_2$ -P25 nanocomposite shell coatings, enhances photocatalytic activity for dye degradation, with the added benefit of easy magnetic separation and recycling, Figure 8. The measured high mass normalised dye degradation rates equal or exceed previously reported values for magnetically separable micron size photocatalytic particles tested under comparable reaction conditions.<sup>33,34,36,37,40,42</sup> Furthermore, the present magnetically separable photocatalysts are much cheaper, simpler to prepare, and readily scalable. All of these factors make them suitable for

local manufacture and adoption in developing countries for sustainable water purification.

## **5. CONCLUSIONS**

TiO<sub>2</sub> nanocomposite coated silica-steel microcomposite core particles have been synthesised using a low-cost and easily scalable sol-gel method. These photocatalysts display high organic dye molecule degradation activities as well as ease of recyclability by magnetic separation from aqueous solution. A synergistic effect upon photocatalytic activity has been found involving level of TiO<sub>2</sub> nanoparticle loading and surface area of the TiO<sub>2</sub> nanocomposite shell coating

## **6. ACKNOWLEDGEMENTS**

We wish to thank Engineering and Physical Sciences Research Council (EPSRC – grant reference EP/J005401/1 and studentship reference EP/K502832/1–DT613210).

## 7. REFERENCES

- [1] United Nations Water. <http://www.unwater.org/statistics/statistics-detail/en/c/260727/> (accessed Feb 22, 2016).
- [2] Almasri, M. N. Nitrate Contamination of Groundwater: A Conceptual Management Framework. *Environ. Impact Assess. Rev.* **2007**, *27*, 220–242.
- [3] Jeevanandam, M.; Kannan, R.; Srinivasalu, S.; Rammohan, V. Hydrogeochemistry and Groundwater Quality Assessment of Lower Part of the Ponnaiyar River Basin, Cuddalore District, South India. *Environ. Monit. Assess.* **2007**, *132*, 263–274.
- [4] Capel, P. D.; Larson, S. J.; Winterstein, T. A. The Behaviour of 39 Pesticides in Surface Waters as a Function of Scale. *Hydrol. Process.* **2001**, *15*, 1251–1269.
- [5] Claver, A.; Ormad, P.; Rodríguez, L.; Ovelleiro, J. L. Study of the Presence of Pesticides in Surface Waters in the Ebro River Basin (Spain). *Chemosphere* **2006**, *64*, 1437–1443.
- [6] Stehle, S.; Schulz, R. Agricultural Insecticides Threaten Surface Waters at the Global Scale. *Proc. Natl. Acad. Sci. USA* **2015**, *112*, 5750–5755.
- [7] McDuffie, H. H.; Pahwa, P.; McLaughlin, J. R.; Spinelli, J. J.; Fincham, S.; Dosman, J. A.; Robson, D.; Skinnider, L. F.; Choi, N. W. Non-Hodgkin's Lymphoma and Specific Pesticide Exposures in Men: Cross-Canada Study of Pesticides and Health. *Cancer Epidemiol. Biomarkers Prev.* **2001**, *10*, 1155–1163.
- [8] Betarbet, R.; Sherer, T. B.; MacKenzie, G.; Garcia-Osuna, M.; Panov, A. V.; Greenamyre, J. T. Chronic Systemic Pesticide Exposure Reproduces Features of Parkinson's Disease. *Nat. Neurosci.* **2000**, *3*, 1301–1306.
- [9] Kamel, F.; Tanner, C. M.; Umbach, D. M.; Hoppin, J. A.; Alavanja, M. C. R.; Blair, A.; Comyns, K.; Goldman, S. M.; Korell, M.; Langston, J. W.; Ross, G. W.; Sandler, D. P. Pesticide Exposure and Self-Reported Parkinson's Disease in the Agricultural Health Study. *Am. J. Epidemiol.* **2007**, *165*, 364–374.
- [10] Eskenazi, B.; Bradman, A.; Castorina, R. Exposures of Children to Organophosphate Pesticides and their Potential Adverse Health Effects. *Environ. Health Persp.* **1999**, *107*, 409–419.
- [11] Brown, D. Effects of Colorants in the Aquatic Environment. *Ecotox. Environ. Safe.* **1987**, *13*, 139–147.
- [12] Geenpeace. <http://www.greenpeace.to/greenpeace/wp-content/uploads/2013/04/Technical-Report-02-2013.pdf> (accessed Mar 1, 2016).
- [13] Geenpeace. <http://www.greenpeace.to/greenpeace/wp-content/uploads/2012/12/TechnicalReport-07-2012.pdf> (accessed Mar 1, 2016).
- [14] Geenpeace. <http://www.greenpeace.to/greenpeace/wp-content/uploads/2012/03/Argentina-tanneries-Technical-Note-07-2011-final.pdf> (accessed Mar 1, 2016).
- [15] de Lima, R. O. A.; Bazo, A. P.; Salvadori, D. M. F.; Rech, C. M.; Oliveira, D. D.; Umbuzeiro, G. D. Mutagenic and Carcinogenic Potential of a Textile Azo Dye Processing Plant Effluent That Impacts a Drinking Water Source. *Mutat. Res-Gen. Tox. En.* **2007**, *626*, 53–60.
- [16] Tsuboy, M. S.; Angeli, J. P. F.; Mantovani, M. S.; Knasmüller, S.; Umbuzeiro, G. A.; Ribeiro, L. R. Genotoxic, Mutagenic and Cytotoxic Effects of the Commercial Dye CI

- Disperse Blue 291 in the Human Hepatic Cell Line HepG2. *Toxicol. In Vitro* **2007**, *21*, 1650–1655.
- [17] Sumathi, M.; Kalaiselvi, K.; Palanivel, M.; Rajaguru, P. Genotoxicity of Textile Dye Effluent on Fish (*Cyprinus Carpio*) Measured Using the Comet Assay. *Bull. Environ. Contam. Toxicol.* **2001**, *66*, 407–414.
- [18] Birhanli, A.; Ozmen, M. Evaluation of the Toxicity and Teratogenity of Six Commercial Textile Dyes Using the Frog Embryo Teratogenesis Assay-Xenopus. *Drug Chem. Toxicol.* **2005**, *28*, 51–65.
- [19] Matthews R. W.; Abdullah M.; Low G. K.-C. Photocatalytic Oxidation for Total Organic-Carbon Analysis. *Anal. Chim. Acta* **1990**, *233*, 171–179.
- [20] Matthews R. W. Purification of Water with Near-UV Illuminated Suspensions of Titanium-Dioxide. *Water Res.* **1990**, *24*, 653–660.
- [21] Low G. K.-C.; McEvoy S. R.; Matthews R. W. Formation of Ammonium and Nitrate Ions from Photocatalytic Oxidation of Ring Nitrogenous Compounds over Titanium Dioxide. *Chemosphere* **1989**, *19*, 1611–1621.
- [22] Low G. K.-C.; McEvoy S. R.; Matthews R. W. Formation of Nitrate and Ammonium-Ions in Titanium-Dioxide Mediated Photocatalytic Degradation of Organic-Compounds Containing Nitrogen-Atoms. *Environ. Sci. Technol.* **1991**, *25*, 460–467.
- [23] Augugliaro, V.; Palmisano, L.; Schiavello, M.; Sclafani, A.; Marchese, L.; Martra, G.; Miano, F. Photocatalytic Degradation of Nitrophenols in Aqueous Titanium-Dioxide Dispersion. *Appl. Catal.* **1991**, *69*, 323–340.
- [24] Jacoby, W. A.; Maness, P. C.; Wolfrum, E. J.; Blake, D. M.; Fennell, J. A. Mineralization of Bacterial Cell Mass on a Photocatalytic Surface in Air. *Environ. Sci. Technol.* **1998**, *32*, 2650–2653.
- [25] Ireland, J. C.; Klostermann, P.; Rice, E. W.; Clark, R. M. Inactivation of *Escherichia Coli* by Titanium-Dioxide Photocatalytic Oxidation. *Appl. Environ. Microbiol.* **1993**, *59*, 1668–1670.
- [26] Saito, T.; Iwase, T.; Horie, J.; Morioka, T. Mode of Photocatalytic Bactericidal Action of Powdered Semiconductor  $\text{TiO}_2$  on Mutans Streptococci. *J. Photochem. Photobiol. B: Biol.* **1992**, *14*, 369–379.
- [27] Matsunaga, T.; Tomoda, R.; Nakajima, T.; Wake, H. Photoelectrochemical Sterilization of Microbial-Cells by Semiconductor Powders. *FEMS Microbiol. Lett.* **1985**, *29*, 211–214.
- [28] Nel, A. E. ; Mädler, L. ; Velegol, D. ; Xia, T. ; Hoek, E. M. V.; Somasundaran, P.; Klaessig, F.; Castranova, V.; Thompson, M. Understanding Biophysicochemical Interactions at the Nano-Bio Interface. *Nat. Mater.* **2009**, *8*, 543–557.
- [29] Bolis, V.; Busco, C.; Ciarletta, M.; Distasi, D.; Erriguez, J.; Fenoglio, I.; Livraghi, S.; Morel, S. Hydrophilic/Hydrophobic Features of  $\text{TiO}_2$  Nanoparticles as a Function of Crystal Phase, Surface Area and Coating, in Relation to their Potential Toxicity in Peripheral Nervous System. *J. Colloid Interface Sci.* **2012**, *369*, 28–39.
- [30] Long, T. C.; Saleh, N.; Tilton, R. D.; Lowry, G. V.; Veronesi, B. Titanium Dioxide (P25) Produces Reactive Oxygen Species in Immortalized Brain Microglia (BV2): Implications for Nanoparticle Neurotoxicity. *Environ. Sci. Technol.* **2006**, *40*, 4346–4352.
- [31] Gurr, J.-R.; Wang, A. S. S.; Chen, C.-H.; Jan, K.-Y. Ultrafine Titanium Dioxide Particles in the Absence of Photoactivation can Induce Oxidative Damage to Human Bronchial Epithelial Cells. *Toxicology* **2005**, *213*, 66–73.

- [32] Tawkaew, S.; Supothina, S. Preparation of Agglomerated Particles of TiO<sub>2</sub> and Silica-Coated Magnetic Particle. *Mater. Chem. Phys.* **2008**, *108*, 147–153
- [33] Wang, Z.; Shen, L.; Zhu, S. Synthesis of Core-Shell Fe<sub>3</sub>O<sub>4</sub>@SiO<sub>2</sub>@TiO<sub>2</sub> Microspheres and Their Application as Recyclable Photocatalysts. *Int. J. Photoenergy* [Online] **2012**, *2012*, Article ID 202519. <http://www.hindawi.com/journals/ijp/2012/202519/cta/> (accessed Feb 22, 2016).
- [34] Liu, R.; Wu, C. F.; Ger, M. D. Degradation of FBL Dye Wastewater by Magnetic Photocatalysts from Scraps. *J. Nanomater.* [Online] **2015**, *2015*, Article ID 651021. <http://www.hindawi.com/journals/jnm/2015/651021/abs/> (accessed Feb 4, 2016).
- [35] Chen, A.; Zeng, G.; Chen, G.; Hu, X.; Yan, M.; Guan, S.; Shang, C.; Lu, L.; Zou, Z.; Xie, G. Novel Thiourea-Modified Magnetic Ion-Imprinted Chitosan/TiO<sub>2</sub> Composite for Simultaneous Removal of Cadmium and 2,4-Dichlorophenol. *Chem. Eng. J.* **2012**, *191*, 85–94.
- [36] Chen, Y.-H.; Liu, Y.-Y.; Lin, R.-H.; Yen, F.-S. Photocatalytic Degradation of p-Phenylenediamine with TiO<sub>2</sub>-Coated Magnetic PMMA Microspheres in an Aqueous Solution. *J. Hazard. Mater.* **2009**, *163*, 973–981.
- [37] Baiyila, D.; Wang, X.; Li, X.; Sharileadolu, B.; Li, X.; Xu, L.; Liu, Z.; Duan, L.; Liu, J. Electrospun TiO<sub>2</sub> Nanofibers Integrating Space-Separated Magnetic Nanoparticles and Heterostructures for Recoverable and Efficient Photocatalyst. *J. Mater. Chem. A* **2014**, *2*, 12304–12310.
- [38] Horikoshi, S.; Serpone, N.; Hisamatsu, Y.; Hidaka, H. Photocatalyzed Degradation of Polymers in Aqueous Semiconductor Suspensions. 3. Photooxidation of a Solid Polymer: TiO<sub>2</sub>-Blended Poly(Vinyl Chloride) Film. *Environ. Sci. Technol.* **1998**, *32*, 4010–4016.
- [39] Allen, N. S.; Bullen, D. J.; McKellar, J. F. Photooxidation of Commercial Polyethylene Containing Titanium-Dioxide (Rutile) - Antioxidant Systems. *J. Mater. Sci.* **1977**, *12*, 1320–1324.
- [40] Li, Z.-Q.; Wang, H.-L.; Zi, L.-Y.; Zhang, J.-J.; Zhang, Y.-S. Preparation and Photocatalytic Performance of Magnetic TiO<sub>2</sub>-Fe<sub>3</sub>O<sub>4</sub>/Graphene (RGO) Composites Under VIS-Light Irradiation. *Ceram. Int.* **2015**, *41*, 10634–10643.
- [41] Li, C.-J.; Wang, J.-N.; Li, X.-Y.; Zhang, L.-L. Functionalization of Electrospun Magnetically Separable TiO<sub>2</sub>-Coated SrFe<sub>12</sub>O<sub>19</sub> Nanofibers: Strongly Effective Photocatalyst and Magnetic Separation. *J. Mater. Sci.* **2011**, *46*, 2058–2063.
- [42] Miranda, L. D. L.; Bellato, C. R.; Milagres, J. L.; Moura, L. G.; Munteer, A. H.; de Almeida, M. F. Hydrotalcite-TiO<sub>2</sub> Magnetic Iron Oxide Intercalated with the Anionic Surfactant Dodecylsulfate in the Photocatalytic Degradation of Methylene Blue Dye. *J. Environ. Manage.* **2015**, *156*, 225–235.
- [43] Hench, L. L.; West, J. K. The Sol-Gel Process. *Chem. Rev.* **1990**, *90*, 33–72.
- [44] Stober, W.; Fink, A.; Bohn, E. Controlled Growth of Monodisperse Silica Spheres in Micron Size Range. *J. Colloid Interface Sci.* **1968**, *26*, 62–69.
- [45] Wang, C.-C.; Ying, J. Y. Sol-Gel Synthesis and Hydrothermal Processing of Anatase and Rutile Titania Nanocrystals. *Chem. Mater.* **1999**, *11*, 3113–3120.
- [46] Nakanishi, K.; Takahashi, R.; Nagakane, T.; Kitayama, K.; Koheiya, N.; Shikata, H.; Soga, N. Formation of Hierarchical Pore Structure in Silica Gel. *J. Sol-Gel Sci. Technol.* **2000**, *17*, 191–210.

- [47] Balasubramanian, G.; Dionysiou, D. D.; Suidan, M. T.; Subramanian, Y.; Baudin, I.; Laine, J.-M. Titania Powder Modified Sol-Gel Process for Photocatalytic Applications. *J. Mater. Sci.* **2003**, *38*, 823–831.
- [48] Chen, F.; Zhao, J. Preparation and Photocatalytic Properties of a Novel Kind of Loaded Photocatalyst of  $\text{TiO}_2/\text{SiO}_2/\gamma\text{-Fe}_2\text{O}_3$ . *Catal. Lett.* **1999**, *58*, 245–247.
- [49] Beydoun, D.; Amal, R.; Low, G.; McEvoy, S. Occurrence and Prevention of Photodissolution at the Phase Junction of Magnetite and Titanium Dioxide. *J. Mol. Catal. A: Chem.* **2002**, *180*, 193–200.
- [50] Houas, A.; Lachheb, H.; Ksibi, M.; Elaloui, E.; Guillard, C.; Herrmann, J.-M. Photocatalytic Degradation Pathway of Methylene Blue in Water. *Appl. Catal. B: Environ.* **2001**, *31*, 145–157.
- [51] Matthews, R. W. Photocatalytic Oxidation and Adsorption of Methylene Blue on Thin Films of Near-Ultraviolet-Illuminated  $\text{TiO}_2$ . *J. Chem. Soc., Faraday Trans. 1* **1989**, *85*, 1291–1302.
- [52] Greenpeace. <http://www.greenpeace.to/greenpeace/wp-content/uploads/2015/05/Pesticides-and-our-Health.pdf> (accessed Mar 1, 2016).
- [53] Barbeni, M.; Pramauro, E.; Pelizzetti, E.; Borgarello, E.; Serpone, N.; Jamieson, M. A. Photochemical Degradation of Chlorinated Dioxins, Biphenyls Phenols and Benzene on Semiconductor Dispersion. *Chemosphere* **1986**, *15*, 1913–1916.
- [54] Barbeni, M.; Pramauro, E.; Pelizzetti, E.; Borgarello, E.; Serpone, N. Photodegradation of Pentachlorophenol Catalyzed by Semiconductor Particles. *Chemosphere* **1985**, *14*, 195–208.
- [55] Matthews, R. W. Photooxidation of Organic Material in Aqueous Suspensions of Titanium-Dioxide. *Water Res.* **1986**, *20*, 569–578.
- [56] Ehrlich, C. D.; Basford, J. A. Recommended Practices for the Calibration and Use of Leaks. *J. Vac. Sci. Technol. A* **1992**, *10*, 1–17.
- [57] Evonik Industries. <https://www.aerosil.com/sites/lists/IM/Documents/TI-1243-Titanium-Dioxide-as-Photocatalyst-EN.pdf> (accessed Jul 8, 2015).
- [58] Brunauer, S.; Emmett, P. H.; Teller, E. Adsorption of Gases in Multimolecular Layers. *J. Am. Chem. Soc.* **1938**, *60*, 309–319.
- [59] Lewis, G. N.; Bigeleisen, J. Methylene Blue and Other Indicators in General Acids. The Acidity Function. *J. Am. Chem. Soc.* **1943**, *65*, 1144–1150.
- [60] Tanuma, S.; Powell, C. J.; Penn, D. R. Calculations of Electron Inelastic Mean Free Paths. 3. Data for 15 Inorganic-Compounds Over the 50-2000-eV Range. *Surf. Interface Anal.* **1991**, *17*, 927–939.
- [61] Cumpson, P. J.; Seah, M. P. Elastic Scattering Corrections in AES and XPS .2. Estimating Attenuation Lengths and Conditions Required for Their Valid Use in Overlayer/Substrate Experiments. *Surf. Interface Anal.* **1997**, *25*, 430–446.
- [62] Gimzewski, J. K.; Padalia, B. D.; Affrossman, S.; Watson, L. M.; Fabian, D. J. Reaction of Oxygen and Water with Iron Films Studied by X-Ray Photoelectron Spectroscopy. *Surf. Sci.* **1977**, *62*, 386–396.
- [63] Moulder, J. F.; Stickle, W. F.; Sobol, P. E.; Bomben, K. D. In *Handbook of X-ray Photoelectron Spectroscopy*; Chastain, J., Eds.; Perkin-Elmer Corporation: Minnesota, 1992; pp 45.

- [64] Liu, P.; Kendelewicz, T.; Brown Jr., G. E.; Nelson, E. J.; Chambers, S. A. Reaction of Water Vapour with  $\alpha$ -Al<sub>2</sub>O<sub>3</sub>(0001) and  $\alpha$ -Fe<sub>2</sub>O<sub>3</sub>(0001) Surfaces: Synchrotron X-Ray Photoemission Studies and Thermodynamic Calculations. *Surf. Sci.* **1998**, *417*, 53–65.
- [65] Görlich, E.; Haber, J.; Stoch, A.; Stoch, J. XPS Study of  $\alpha$ -Quartz Surface. *J. Sol. State Chem.* **1980**, *33*, 121–124.
- [66] Paparazzo, E.; Fanfoni, M.; Severini, E.; Priori, S. Evidence of Si-OH Species at the Surface of Aged Silica. In *J. Vac. Sci Technol. A*, 38<sup>th</sup> National Symposium of the American Vacuum Society, Seattle, WA, Nov 11–15, 1991; American Institute of Physics: New York, 1992; pp 2892–2896.
- [67] Colomban, Ph.; Cherifi, S.; Despert, G. Raman Identification of Corrosion Products on Automotive Galvanized Steel Sheets. *J. Raman Spectrosc.* **2008**, *39*, 881–886.
- [68] Colomban, Ph. Raman Studies of Inorganic Gels and of Their Sol-to-Gel, Gel-to-Glass and Glass-to-Ceramics Transformations. *J. Raman Spectrosc.* **1996**, *27*, 747–758.
- [69] Kato, K. Transformation of Alkoxy-Derived SiO<sub>2</sub> Gels Without Catalysts to Glasses. *J. Mater. Sci.* **1991**, *26*, 6777–6781.
- [70] Stolen, R. H.; Walrafen, G. E. Water and its Relation to Broken Bond Defects in Fused Silica. *J. Chem. Phys.* **1976**, *64*, 2623–2631.
- [71] Horiba Application Note.  
[http://www.horiba.com/fileadmin/uploads/Scientific/Documents/Raman/Semiconductors\\_01.pdf](http://www.horiba.com/fileadmin/uploads/Scientific/Documents/Raman/Semiconductors_01.pdf) (accessed Sep 14, 2016)
- [72] Presser, V.; Keuper, M.; Berthold, C.; Nickel, K. G. Experimental Determination of the Raman Sampling Depth in Zirconia Ceramics. *Appl. Spectrosc.* **2009**, *63*, 1288–1292.
- [73] Beattie, I. R.; Gilson, T. R. Single Crystal Laser Raman Spectroscopy. *Proc. Roy. Soc. A.* **1968**, *307*, 407–429.
- [74] Ohsaka, T.; Izumi, F.; Fujiki, Y. Raman-Spectrum of Anatase, TiO<sub>2</sub>. *J. Raman Spec.* **1978**, *7*, 321–324.
- [75] Narayanan, P. S. Raman Spectrum of Rutile: Polarisation Studies. *P. Indian Acad. Sci. A* **1953**, *37*, 411–414.
- [76] Porto, S. P. S.; Fleury, P. A.; Damen, T. C. Raman Spectra of TiO<sub>2</sub>, MgF<sub>2</sub>, ZnF<sub>2</sub>, FeF<sub>2</sub>, and MnF<sub>2</sub>. *Phys. Rev.* **1967**, *154*, 522–526.
- [77] Bickley, R. I.; Gonzalez-Carreno, T.; Lees, J. S.; Palmisano, L.; Tilley, R. J. D. A Structural Investigation of Titanium-Dioxide Photocatalysts. *J. Solid State Chem.* **1991**, *92*, 178–190.
- [78] Swanson, H. E.; McMurdie, H. F.; Morris, M. C.; Evans, E. H. *Standard X-Ray Diffraction Powder Patterns*; National Bureau of Standards Monograph 25 Section 7; National Bureau of Standards: Washington, DC, 1969; pp. 82–83.
- [79] Spurr, R. A.; Myers, H. Quantitative Analysis of Anatase-Rutile Mixtures with an X-Ray Diffractometer. *Anal. Chem.* **1957**, *29*, 760–762.
- [80] Swanson, H. E.; McMurdie, H. F.; Morris, M. C.; Evans, E. H. *Standard X-Ray Diffraction Powder Patterns*; National Bureau of Standards Monograph 25 Section 5; National Bureau of Standards: Washington, DC, 1969; pp. 31.
- [81] Morris, M. C.; McMurdie, H. F.; Evans, E. H.; Paretzkin, B.; Parker, H. S.; Panagiotopoulos, N. C. *Standard X-Ray Diffraction Powder Patterns*; National Bureau of Standards Monograph 25 Section 18; National Bureau of Standards: Washington, DC, 1969; pp. 37.

- [82] Naldoni, A.; Allieta, M.; Santangelo, S.; Marelli, M.; Fabbri, F.; Cappelli, S.; Bianchi, C. L.; Psaro, R.; Dal Santo, V. Effect of Nature and Location of Defects on Bandgap Narrowing in Black TiO<sub>2</sub> Nanoparticles. *J. Am. Chem. Soc.* **2012**, *134*, 7600–7603.
- [83] Knorr, F. J.; Zhang, D.; McHale, J. L. Influence of TiCl<sub>4</sub> Treatment on Surface Defect Photoluminescence in Pure and Mixed-Phase Nanocrystalline TiO<sub>2</sub>. *Langmuir*, **2007**, *23*, 8686–8690.
- [84] Tang, H.; Prasad, K.; Sanjinès, R.; Schmid, P. E.; Lévy, F. Electrical and Optical Properties of TiO<sub>2</sub> Anatase Thin Films. *J. Appl. Phys.* **1994**, *75*, 2042–2047.
- [85] Nagaveni, K.; Hegde, M. S.; Ravishankar, N.; Subbanna, G. N.; Madras, G. Synthesis and Structure of Nanocrystalline TiO<sub>2</sub> with Lower Band Gap Showing High Photocatalytic Activity. *Langmuir* **2004**, *20*, 2900–2907.
- [86] Murphy, A. B. Band-gap Determination from Diffuse Reflectance Measurements of Semiconductor Films, and Application to Photoelectrochemical Water-Splitting. *Sol. Energ. Mat. Sol. Cells* **2007**, *91*, 1326–1337.
- [87] Chen, X.; Liu, L.; Yu, P. Y.; Mao, S. S. Increasing Solar Absorption for Photocatalysis with Black Hydrogenated Titanium Dioxide Nanocrystals. *Science* **2011**, *331*, 746–750.
- [88] Tada, H.; Tanaka, M. Dependence of TiO<sub>2</sub> Photocatalytic Activity upon its Film Thickness. *Langmuir* **1997**, *13*, 360–364.
- [89] Riegel G.; Bolton J. R. Photocatalytic Efficiency Variability in TiO<sub>2</sub> Particles. *J. Phys. Chem.* **1995**, *99*, 4215–4224.
- [90] Munuera, G.; Rives-Arnau, V.; Saucedo, A. Photo-Adsorption and Photo-Desorption of Oxygen on Highly Hydroxylated TiO<sub>2</sub> Surfaces. Part 1. – Role of Hydroxyl Groups in Photo-Adsorption. *J. Chem. Soc., Faraday Trans.* **1979**, *75*, 736–747.
- [91] Gerischer, H. Photoelectrochemical Catalysis of the Oxidation of Organic Molecules by Oxygen on Small Semiconductor Particles with TiO<sub>2</sub> as an Example. *Electrochim. Acta* **1993**, *38*, 3–9.
- [92] Howe, R. F.; Grätzel, M. EPR Observation of Trapped Electrons in Colloidal Titanium Dioxide. *J. Phys. Chem.* **1985**, *89*, 4495–4499.
- [93] Henderson, M. A.; Epling, W. S.; Peden, C. H. F. Perkins, C. L. Insights into Photoexcited Electron Scavenging Processes on TiO<sub>2</sub> Obtained from Studies of the Reaction of O<sub>2</sub> with OH Groups Adsorbed at Electronic Defects on TiO<sub>2</sub>(110). *J. Phys. Chem. B* **2003**, *107*, 534–545.
- [94] Anpo, M.; Che, M.; Fubini, B.; Garrone, E.; Giamello, E.; Paganini, M. C. Generation of Superoxide Ions at Oxide Surfaces. *Top. Catal.* **1999**, *8*, 189–198.
- [95] Anpo, M.; Chiba, K.; Tomonari, M.; Coluccia, S.; Che, M.; Fox, M. A. Photocatalysis on Native and Platinum-Loaded TiO<sub>2</sub> and ZnO Catalysts — Origin of Different Reactivities on Wet and Dry Metal Oxides —. *Bull. Chem. Soc. Jpn.* **1991**, *64*, 543–551.
- [96] Okamoto, K.; Yamamoto, Y.; Tanaka, H.; Itaya, A. Kinetics of Heterogeneous Photocatalytic Decomposition of Phenol over Anatase TiO<sub>2</sub> Powder. *Bull. Chem. Soc. Jpn.* **1985**, *58*, 2023–2028.
- [97] Okamoto, K.; Yamamoto, Y.; Tanaka, H.; Tanaka, M.; Itaya, A. Heterogeneous Photocatalytic Decomposition of Phenol over TiO<sub>2</sub> Powder. *Bull. Chem. Soc. Jpn.* **1985**, *58*, 2015–2022.
- [98] Turchi, C. S.; Ollis, D. F. Photocatalytic Degradation of Organic Water Contaminants: Mechanisms Involving Hydroxyl Radical Attack. *J. Catal.* **1990**, *112*, 178–192.

- [99] Draper, R. B.; Fox, M. A. Titanium Dioxide Photosensitized Reactions Studied by Diffuse Reflectance Flash Photolysis in Aqueous Suspensions of TiO<sub>2</sub> Powder. *Langmuir* **1990**, *6*, 1396–1402.
- [100] Beydoun, D.; Amal, R.; Low, G. K. C.; McEvoy, S. Novel Photocatalyst: Titania-Coated Magnetite. Activity and Photodissolution. *J. Phys. Chem. B* **2000**, *104*, 4387–4396.
- [101] Narayani, H.; Arayapurath, H.; Shukla, S. Using Fenton-Reaction as a Novel Approach to Enhance the Photocatalytic Activity of TiO<sub>2</sub>-γ-Fe<sub>2</sub>O<sub>3</sub> Magnetic Photocatalyst Undergoing Photo-Dissolution Process without Silica Interlayer. *Catal. Lett.* **2013**, *143*, 807–816.
- [102] Anderson, M. A.; Gieselmann, M. J.; Xu, Q. Titania and Alumina Ceramic Membranes. *J. Membr. Sci.* **1988**, *39*, 243–258.
- [103] Zhang, H.; Banfield, J. F. Thermodynamic Analysis of Phase Stability of Nanocrystalline Titania. *J. Mater. Chem.* **1998**, *8*, 2073–2076.
- [104] Zhang, H.; Banfield, J. K. Understanding Polymorphic Phase Transformation Behavior during Growth of Nanocrystalline Aggregates: Insights from TiO<sub>2</sub>. *J. Phys. Chem. B* **2000**, *104*, 3481–3487.
- [105] Naicker, P. K.; Cummings, P. T.; Zhang, H.; Banfield, J. F. Characterization of Titanium Dioxide Nanoparticles Using Molecular Dynamics Simulations. *J. Phys. Chem. B* **2005**, *109*, 15243–15249.
- [106] Navrotsky, A. Energetics of Nanoparticle Oxides: Interplay Between Surface Energy and Polymorphism. *Geochem. Trans.* **2003**, *4*, 34–37.
- [107] Yanagisawa, K.; Ovenstone, J. Crystallization of Anatase from Amorphous Titania Using the Hydrothermal Technique: Effects of Starting Material and Temperature. *J. Phys. Chem. B* **1999**, *103*, 7781–7787.
- [108] Yanagisawa, K.; Yamamoto, Y.; Feng, Q.; Yamasaki, N. Formation Mechanism of Fine Anatase Crystals from Amorphous Titania under Hydrothermal Conditions *J. Mater. Res.* **1998**, *13*, 825–829.
- [109] Chen, Y.; Dionysiou, D. D. TiO<sub>2</sub> Photocatalytic Films on Stainless Steel: The Role of Degussa P-25 in Modified Sol–Gel Methods. *Appl. Catal. B: Environ.* **2006**, *62*, 255–264.
- [110] Jing, L.; Li, S.; Song, S.; Xue, L.; Fu, H. Investigation on the Electron Transfer Between Anatase and Rutile in Nano-Sized TiO<sub>2</sub> by Means of Surface Photovoltage Technique and its Effects on the Photocatalytic Activity. *Sol. Energ. Mat. Sol. Cells* **2008**, *92*, 1030–1036.
- [111] Hurum, D. C.; Agrios, A. G.; Gray, K. A.; Rajh, T.; Thurnauer, M. C. Explaining the Enhanced Photocatalytic Activity of Degussa P25 Mixed-Phase TiO<sub>2</sub> Using EPR. *J. Phys. Chem. B* **2003**, *107*, 4545–4549.

**MAGNETIC RECYCLABLE MICROCOMPOSITE SILICA-STEEL  
CORE WITH TiO<sub>2</sub> NANOCOMPOSITE SHELL PHOTOCATALYSTS  
FOR SUSTAINABLE WATER PURIFICATION**

**(Supplementary Material)**

M. Wilson, C. Y. C. Cheng, G. Oswald, R. Srivastava<sup>a</sup>, S. K. Beaumont, and J. P. S.  
Badyal\*

Department of Chemistry  
Science Laboratories  
Durham University  
Durham DH1 3LE  
England, UK

<sup>a</sup> Department of Chemistry, Indian Institute of Technology Ropar, Punjab 140001,  
India

\* Corresponding author email: [j.p.badyal@durham.ac.uk](mailto:j.p.badyal@durham.ac.uk)

## 1. FIGURES

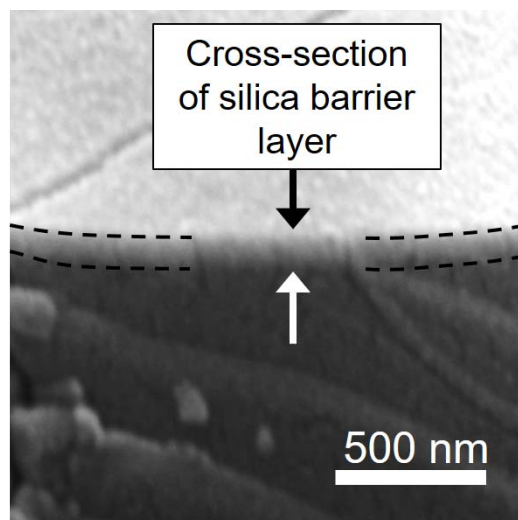


Figure S1: Cross sectional SEM micrograph of a quartz slide coated with a double silica barrier layer taken at  $10^\circ$  from parallel to the electron beam path.

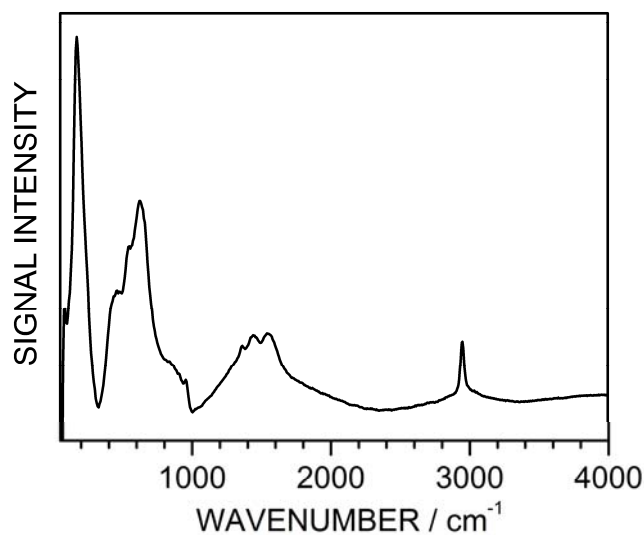


Figure S2: Raman spectra of uncalcined  $\text{TiO}_2(1)$  particles. The absorbance at  $448 \text{ cm}^{-1}$  can be assigned to disordered  $\text{TiO}_2$ ,<sup>1,2</sup> (any adsorbed water librational bands typically appear around the  $450 \text{ cm}^{-1}$  region<sup>3</sup>). The peak at  $182 \text{ cm}^{-1}$  may be due to overlapping Raman active modes (including hydrogen bonded water vibrational bands at  $175 \text{ cm}^{-1}$ ,<sup>3</sup> and bridging hydroxyl group vibrational bands around  $265 \text{ cm}^{-1}$  in sheet silica<sup>4</sup>). The signal at  $2966 \text{ cm}^{-1}$  stems from residual acetic acid present in the film from the dip coating solution.<sup>5</sup>

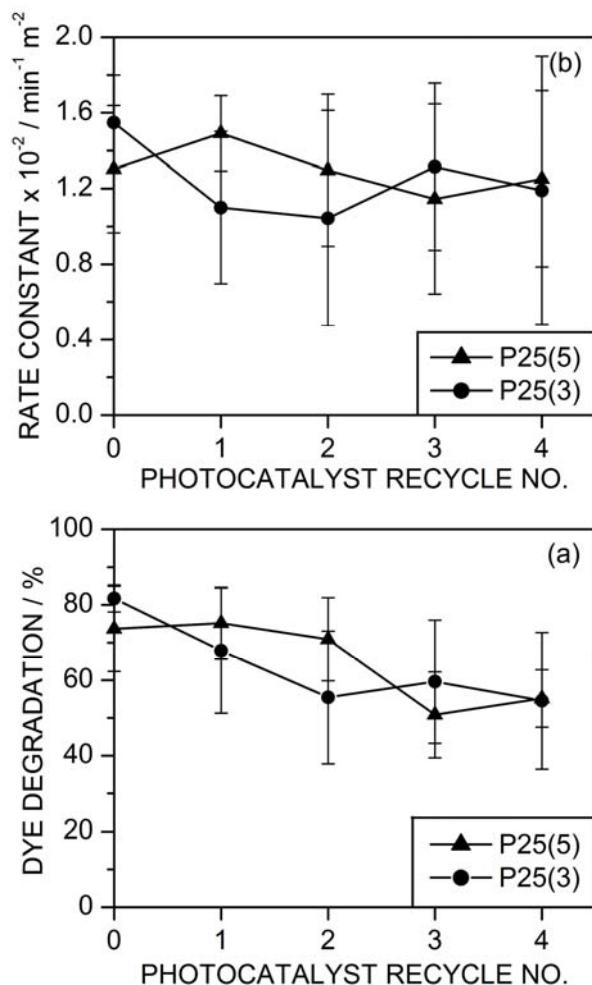


Figure S3: Magnetic separation recycling study using silica-steel microcomposite core with  $\text{TiO}_2$ -P25 nanocomposite shell photocatalyst particles (loading of  $2.0 \pm 0.3 \text{ mg mL}^{-1}$ ) for UV degradation of methylene blue dye solution ( $4 \mu\text{M}$ ): (a) percentage of dye degraded after 30 min continuous UV irradiation; and (b) dye photodegradation rate normalised to surface area (the large error values are due to propagation of error from surface area measurements). All photodegradation rates of the methylene blue dye solution using the photocatalyst particles were measured following an initial equilibration period in the dark for 1 h (see Figure 7). The background UV degradation rate ( $0.59 \pm 0.15 \times 10^{-2} \text{ min}^{-1}$ ) of methylene blue dye measured in the absence of any photocatalyst particles has been subtracted prior to surface area normalisation in all cases.

## 2. TABLE

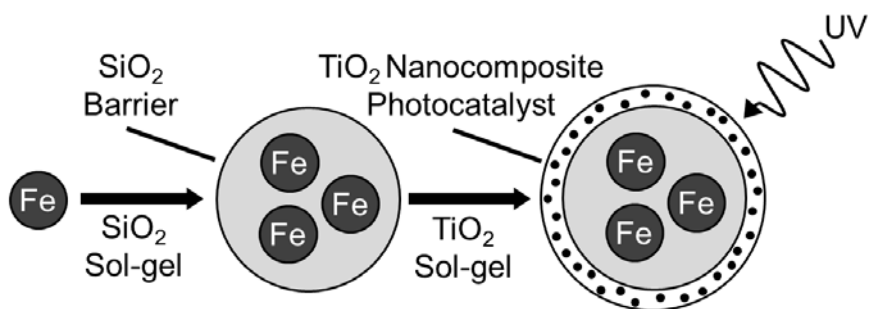
Table S1: Assignment of Raman bands for uncoated and coated steel particles.

Uncoated		Silica Double Barrier Layer	
Peak Position / cm <sup>-1</sup>	Assignment <sup>6</sup>	Peak Position / cm <sup>-1</sup>	Assignment <sup>6,7,8</sup>
213	Haematite Fe <sub>2</sub> O <sub>3</sub>	210	Haematite Fe <sub>2</sub> O <sub>3</sub>
281	Haematite Fe <sub>2</sub> O <sub>3</sub>	279	Haematite Fe <sub>2</sub> O <sub>3</sub>
395	Haematite Fe <sub>2</sub> O <sub>3</sub>	495	SiO <sub>2</sub> Defect peak
593	Haematite Fe <sub>2</sub> O <sub>3</sub>	1005	SiO <sub>2</sub>
645	Magnetite Fe <sub>3</sub> O <sub>4</sub>	1365	SiO <sub>2</sub>
1252	Haematite Fe <sub>2</sub> O <sub>3</sub>		
TiO <sub>2</sub> (1)		P25(5) Coated Steel Particles	
Peak Position / cm <sup>-1</sup>	Assignment <sup>6,9,10</sup>	Peak Position / cm <sup>-1</sup>	Assignment <sup>9,10</sup>
141	Anatase Eg	148	Anatase Eg
291	Haematite Fe <sub>2</sub> O <sub>3</sub>	398	Anatase B <sub>1g</sub>
397	Anatase B <sub>1g</sub>	516	Anatase A <sub>1g</sub> or B <sub>1g</sub>
517	Anatase A <sub>1g</sub> or B <sub>1g</sub>	638	Anatase Eg
637	Anatase Eg		
P25 TiO <sub>2</sub> Nanoparticles			
Peak position / cm <sup>-1</sup>	Assignment <sup>9,10</sup>		
148	Anatase Eg		
394	Anatase B <sub>1g</sub>		
513	Anatase A <sub>1g</sub> or B <sub>1g</sub>		
636	Anatase Eg		

### 3. REFERENCES

- [1] Hsu, L. S.; Rujkorakarn, R.; Sites, J. R.; She, C. Y. Thermally Induced Crystallization of Amorphous-Titania Films. *J. Appl. Phys.* **1986**, *59*, 3475–3480.
- [2] Exarhos, G. J.; Hess, N. J. Phase Transformation Dynamics, Melting and Stress Evolution in Dielectric Films and at Surfaces. *J. Raman Spectrosc.* **1996**, *27*, 765–774.
- [3] Walrafen, G. E. Raman Spectral Studies of Water Structure. *J. Chem. Phys.* **1964**, *40*, 3249–3256.
- [4] Loh, E. Optical Vibrations in Sheet Silicates. *J. Phys. C. Solid State Phys.* **1973**, *6*, 1091–1104.
- [5] Nakabayashi, T.; Kosugi, K.; Nishi, N. Liquid Structure of Acetic Acid Studied by Raman Spectroscopy and Ab Initio Molecular Orbital Calculations. *J. Phys. Chem. A* **1999**, *103*, 8595–8603.
- [6] Colomban, Ph.; Cherifi, S.; Despert, G. Raman Identification of Corrosion Products on Automotive Galvanized Steel Sheets. *J. Raman Spectrosc.* **2008**, *39*, 881–886.
- [7] Kato, K. Transformation of Alkoxy-Derived SiO<sub>2</sub> Gels Without Catalysts to Glasses. *J. Mater. Sci.* **1991**, *26*, 6777–6781.
- [8] Stolen, R. H.; Walrafen, G. E. Water and its Relation to Broken Bond Defects in Fused Silica. *J. Chem. Phys.* **1976**, *64*, 2623–2631.
- [9] Beattie, I. R.; Gilson, T. R. Single Crystal Laser Raman Spectroscopy. *Proc. Roy. Soc. A.* **1968**, *307*, 407–429.
- [10] Ohsaka, T.; Izumi, F.; Fujiki, Y. Raman-Spectrum of Anatase, TiO<sub>2</sub>. *J. Raman Spec.* **1978**, *7*, 321–324.

# GRAPHICAL ABSTRACT



## **HIGHLIGHTS**

- Micron sized silica-steel microcomposite core with TiO<sub>2</sub> nanocomposite shell photocatalysts.
- Recycling from solution by magnetic separation.
- UV photocatalytic degradation of waterborne organic pollutants.